The Pennsylvania State University

The Graduate School

College of Engineering

NONLINEAR OPTICAL IMAGING AND SPECTROSCOPY WITH ULTRAFAST LASER PULSES

A Dissertation in

Electrical Engineering

by

Chuan Yang

Submitted in Partial Fulfillment

of the Requirements

for the Degree of

Doctor of Philosophy

August 2013

The dissertation of Chuan Yang was reviewed and approved* by the following:

Zhiwen Liu
Associate Professor of Electrical Engineering
Dissertation Advisor
Chair of Committee

Qiming Zhang
Distinguished Professor of Electrical Engineering

Siyang Zheng
Assistant Professor of Bioengineering

Iam-Choon Khoo
William E. Leonhard Professor of Electrical Engineering

Victor Pasko
Professor of Electrical Engineering
Chair of Graduate Program

*Signatures are on file in the Graduate School

ABSTRACT

In the past several years, my Ph.D. research is mainly focusing on developing techniques for nonlinear optical imaging and spectroscopy. After decades of development, nonlinear optical microscopy modalities are playing a vital role in modern medical and biological research and applications. Conventional nonlinear microscopy is usually too slow for dynamic applications due to its imaging approach of three-dimension (3D) point-by-point scanning. By integrating technologies of nanofabrication, spectroscopy and diffractive optics, we successfully eliminated the mechanical scanning along depth dimension, and therefore the three-dimension nonlinear imaging including second harmonic generation (SHG), two-photon absorption (TPA) and confocal can be significantly expedited. In the chapter 2 of this thesis, I will describe two of my Ph.D. research projects on non-axial-scanning 3D nonlinear imaging. In order to further optimize the performance of nonlinear optical microscopy, fundamental research on light-matter interactions has been intensively carried out. Some other related domains like photon coherent control and laser source optimization can also benefit from this research. Critical information of light-matter interactions is contained in the amplitude and phase information of coherent light. Our group proposed a solution of collinear frequency-resolved optical gating (cFROG) based on a second harmonic nanoprobe (SHARP) for *in situ* characterization of ultrafast laser pulses in the nano-femto spatiotemporal scale. As a further step forward, here we combine holography technique with cFROG method to completely characterize the field and this newly-developed technique has enabled us to obtain detailed information of the pulse propagation. This new technique for spatiotemporal characterization of laser pulse will be detailed in Chapter 3. As the most

used instrument for my experimental research on nonlinear optics, the optical spectrometer is one of the most important and most widely used instruments in various research areas. However, most spectrometers are too expensive or too bulky. Therefore, we developed the prototype of a miniature spectrometer with a single diffractive element that integrates the functions of multiple components installed in a traditional spectrometer. Our palm-size prototype has comparative performance to some existing much-more-expensive commercial spectrometers. In addition, the material for fabricating the device was carefully selected so that the cost can be lowered down significantly. Chapter 4 of my thesis will be focusing on this new prototype instrument we named G-Fresnel spectrometer.

Table of Contents

LIST OF FIGURES

ACKNOWLEDGEMENT

First of all I would like to express my deepest gratitude to my advisor Professor Zhiwen Liu for his unreserved support, guidance, and inspiration throughout my Ph.D. process. His comprehensive knowledge, his enthusiasm and devotion to education, and his patience in guiding me through every obstacle I have encountered in my work and life is greatly appreciated.

Also I am grateful for the inexhaustible instructions and significant amount of hands-on assistance with my research from my former senior colleagues Professor Kebin Shi, Dr. Qian Xu and Dr. Haifeng Li. I also appreciate help from my current labmates and close friends Mr. Perry Edwards, Mr. Nikhil Mehta, Mr. Ding Ma, Mr. Corey Janish, Mr. Chenji Zhang and Mr. Alexander Cocking. I feel incredibly lucky to have these lovely and sincere friends on my rough yet exciting journey of pursuing my Ph.D. degree.

I want to thank Professor Siyang Zheng, Professor Shizhuo Yin, Professor Venkatraman Gopalan and Mr. Mingda Zhou for substantial discussion during our fruitful collaborations.

In the end I feel deeply indebted to my parents for their unconditional support. Without their sacrifice and encouragement, I won't be able to make any achievement. Also I want to thank my forever love Miss Dan Zhong for her continuous support and comfort during my most difficult time of study and career.

CHAPTER 1. INTRODUCTION

Interesting phenomena that the dielectric polarization $\vec{P}$ of the media responses nonlinearly to the applied electric field $\vec{E}$ has triggered intense interest in the research fields categorized as nonlinear optics. This nonlinearity usually emerges when the intensity of the field is comparable to the inter-atomic field of the media. Assuming no dispersion, the relation between dielectric polarization $\vec{P}$ and the externally applied electric field $\vec{E}$, instead of being simply linear, could be described as Eq. 1.1.1 [1].

$$P_i = \varepsilon_0(\chi_{ij}E_j + 2d_{ijk}E_jE_k + 4\chi_{ijkl}E_jE_kE_l + ...) \quad (i,j,k,l = x,y,z) \quad (1.1.1)$$

in which P_i and E_i are the instantaneous $\hat{i}$ components of the dielectric polarization $\vec{P}$ and the incident electric field $\vec{E}$, respectively. χ_{ij} is linear susceptibility. d_{ijk} and χ_{ijkl} are second-order and third-order susceptibilities, respectively. Important processes due to second-order nonlinearity include second harmonic generation (SHG), sum frequency generation (SFG) and difference frequency generation (DFG). Second-order nonlinearity susceptibility only exists in crystals without inversion symmetry under the electric dipole approximation [1]. Important processes due to third-order nonlinearity include Optical Kerr Effect, Stimulated Raman Scattering (SRS), Stimulated Brillouin Scattering (SBS) and Four Wave Mixing (FWM).

In 1931, two-photon absorption was predicted by Maria Goeppert-Mayer in her doctoral dissertation [2]. Not until thirty years later, two-photon excitation was first experimentally observed in $CaF_2 : Eu^{2+}$ crystal by Wolfgang Kaiser [3]. In 1977, Colin J. R. Sheppard *et al.* proposed and demonstrated three-dimension laser-scanning nonlinear optical microscopy [4]. Although his demonstration was based on the second harmonic generation phenomenon, but the idea of establishing imaging contrast by focusing an excitation beam to a small volume to generate highly-localized signal and of forming a three-dimension image by spatially scanning the focal point over specimen has triggered a revolution in optical microscopy in the following decades.

The invention of femtosecond laser in 1980s has significantly boosted the development of nonlinear microscopy. In 1990, Winfried Denk and Watt W. Webb at Cornell University combined two-photon absorption technique together with a laser scanner to first demonstrate the two-photon excitation fluorescence microscopy [5]. Nowadays, two-photon fluorescence microscopy has become a widely used nonlinear technique for biological and medical applications. Compared with conventional one-photon fluorescence imaging, two-photon fluorescence imaging has multiple advantages. For example, due to the longer wavelength used in the two-photon excitation, much deeper penetration depth into the specimen could be achieved. This is a great help for some critical applications like thick tissue

microscopy. Also lower excitation photon energy mitigates the damage to the biological samples. A significant advantage of the two-photon excitation is its inherent optical sectioning capability. Since the probability for two-photon absorption to happen is proportional to the square of the excitation light intensity, only at the tightly focused region of the excitation beam the specimen could be excited effectively. Therefore the out-of-focus signal contributions can be suppressed.

Three-dimension mechanical scanning of either the specimen or the optics is too slow for many of today's applications. During the past years, considerable efforts have been devoted to reduce the image acquisition times of the nonlinear optical microscopy so that various dynamical systems can be monitored in real time to obtain valuable information for various applications in biological and material science. So far, methods of creating multiple foci to generate image signal in parallel have been widely discussed, but most of the progresses are focused on lateral dimensions [6].

In Chapter 2, we will propose a solution of non-axial-scanning three-dimension nonlinear microscopy through an axial multi-focus configuration realized by large chromatic aberration of a diffractive optical element. Because of the chromatic aberration, different wavelengths of the excitation beam are focused at different axial positions of the specimen. In the case of two-photon absorption, fluorescence signals are generated at multiple depths in parallel. By utilizing an array

of 45 °-tilted micro mirrors arranged along the axial direction, image signals emitted from different axial positions can be orthogonally reflected by the corresponding micro mirrors and spatially separated for parallel detection, essentially converting the more challenging axial imaging to a lateral imaging problem. Each micro mirror also provides optical sectioning capability due to its finite dimension. Numerical analysis shows that nearly diffraction limited axial resolution can be achieved. Experimental demonstration of z-imaging of fluorescent microspheres is also presented. In the case of second harmonic imaging microscopy, signal from different axial positions are generated by different fundamental wavelengths and hence accordingly have different center wavelengths. They can be resolved and detected in parallel by using a spectrometer without axial mechanical scanning. Proof-of-concept imaging results are also presented.

In my Ph.D. work, substantial time and efforts have been devoted to the research of nonlinear imaging microscopy. In these projects, the focusing of ultrafast femtosecond pulses with a customized diffractive optical element plays a prominent part in engineering the distribution of the electric fields in the vicinity of focus of the excitation beam inside a nonlinear medium. The performance of our proposed imaging strategies is expected to have a significant enhancement as long as the distribution of the electric field can be further optimized. However, our achievement is restricted by the deficiency of knowledge on the evolution of the spatiotemporal

features of the ultrafast pulse being focused. Therefore, characterization of ultrafast pulses is critical to the further improvement of nonlinear imaging applications. In addition, since pulse shaping techniques have been widely exploited in multiple areas including laser source optimization [7], coherence control [8-11] and laser micromachining [12], the pulse diagnostic techniques are also needed in these areas.

A characterization method termed frequency-resolve optical gating (FROG) was invented by Rick Trebino in 1991 [13, 14], in which the intensity autocorrelation is spectrally resolved and both the intensity profile and phase can be retrieved. With FROG technique, full characterization of pulse with duration down to 4.5 fs was reported [15]. On the other hand, due to the progress of nanotechnology, pulses can be investigated at unprecedented small spatial scale. For example, near-field scanning optical microscopy (NSOM) has been used to measure the optical near fields [16, 17]. However, these implementations require the local mode to be coupled into a propagating mode, which actually may easily distort the pulse.

In Chapter 3, we combine holography technique with collinear FROG method to characterize the field and obtain the group delay of the propagating pulse. Our system is built on a conventional collinear FROG (cFROG) setup [18] with a BBO crystal plugged into the pumping beam path before interferometer to generate a reference beam at second-harmonic wavelength. In the end this reference beam is combined with the cFROG signal to form a spectral hologram that is recorded by the

spectrometer in the frequency domain. By analyzing the resulted holographic cFROG trace at different spatial locations, not only the information of the pulse intensity profile and phase can be retrieved, but also critical properties of the pulse propagation like group delay dispersion can be obtained as well.

As the most critical method for signal analysis throughout my Ph.D. research, optical spectroscopy plays a vital role in many of today's rapidly developing fields in science and engineering. In particular, there exists a growing demand for the development of low-cost and miniature solutions of spectroscopy. Miniaturizing spectrometers allows for easier integration into other instruments such as mobile electronics (cell phones, laptops) and even smaller spectrometer solutions for integration with lab-on-a-chip devices. Despite a steady progress on the spectrometer performance, the use of discrete optical components (i.e., the collimating and collecting curved mirrors and the diffraction grating) has been a main reason that conventional optical spectrometers are usually bulky and costly.

In Chapter 4, a hybrid diffractive optical element termed G-Fresnel is invented and demonstrated, which integrates the functionalities of a grating and a Fresnel lens in a single thin-film device and can both disperse and focus light [19]. In a typical two-sided realization of this device, a grating and a Fresnel lens are respectively fabricated in the opposing sides. The advantages of the G-Fresnel are three-fold: first, it combines the functions of collimation, dispersion and collection in

a single thin-film element; second, it can have a low f-number, leading to a compact system; third, it may be realized by surface relief patterning, opening the possibility of low-cost volume production through replicating from a master pattern.

In Chapter 5, a summary will be provided and recommendations for future work are presented.

CHAPTER 2. NON-AXIAL-SCANNING 3D NONLINEAR IMAGING

2.1 Introduction to two-photon fluorescence imaging

Two-photon absorption was first predicted by Maria Geoppert-Mayer in the year of 1931 in her Ph.D. thesis [2] and was first experimentally verified thirty years later after laser was invented [3]. Two-photon absorption (TPA) is one of the most important nonlinear optical processes in the field of modern nonlinear optical imaging. A molecular can be excited from one state (usually ground state) to a higher energy electronic state by simultaneously absorbing two photons with identical or different frequencies. The energy difference between these two states equals the sum of the energies of the two photons absorbed. In 1990, Winfried Denk and Watt W. Webb at Cornell University combined TPA technique together with a laser scanner to first demonstrate the two-photon excitation fluorescence microscopy [5]. The process of two-photon excitation fluorescence is illustrated by an energy diagram as shown in Fig.2.1.1. After electronic transition from ground state to some vibrational level of the first excited electronic state through TPA via virtual state in between, the fluorophore relaxes to the lowest level of the first excited electronic state. The fluorescent photon is emitted when electron transits down to some vibrational level of the ground state. Due to the existence of multiple vibrational levels in both ground state and excited state, fluorescence process has certain emission and excitation

bandwidths. Because of the extremely short lifetime of the intermediate virtual state, the molecule needs to absorb two excitation photons almost simultaneously, which requires ultra-high spatial density of the excitation photons. A femtosecond laser is an ideal solution for providing such a high flux of excitation photons.

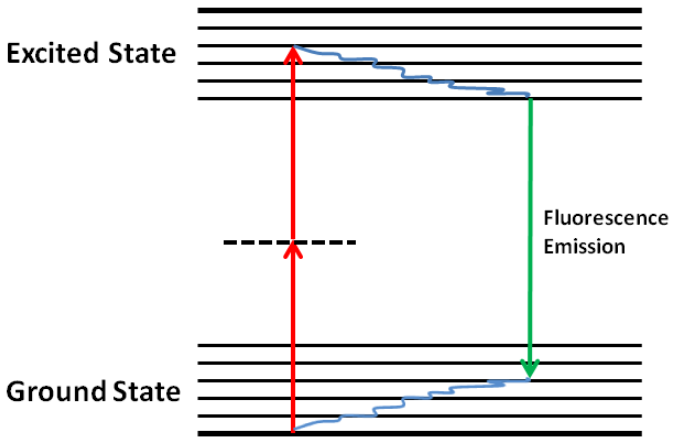

Figure 2.1.1 Schematic representation of two photon excitation fluorescence

Due to the longer wavelength used in the two-photon excitation, much deeper penetration depth into the specimen could be achieved. This is a great help for some critical applications like thick tissue microscopy. Also lower excitation photon energy and "intermittent pumping" of pulsed laser mitigate the damage to the biological samples. A significant advantage of the two-photon excitation is its inherent optical sectioning capability. The probability for two-photon absorption to happen is proportional to the square of the excitation light intensity. As a result, only

at the tightly focused region of the excitation beam the specimen could be excited effectively. Therefore the out-of-focus signal contributions can be suppressed.

2.2 Non-axial-scanning 3D fluorescence imaging

In the research field of conventional wide-field microscopy, multiple solutions were proposed for three-dimensional imaging without axial scanning. For example, multi-focal imaging has been investigated by using multiple cameras with each placed at a different distance to image a different conjugate depth plane inside the sample [20, 21]. Holography has also been applied to fluorescence microscopy to achieve three-dimensional imaging [22]. In the field of laser scanning optical microscopy, multi-photon and confocal microscopy techniques have become widely used imaging modalities due to their unique optical sectioning capability. Miscellaneous techniques are being proposed to acquire images at lateral dimensions in parallel or at high speed, while slow mechanical scanning of the optical elements or the specimen itself is still typically required in the z direction for axial (z) imaging, which impedes the development of the capability for imaging fast processes in the depth direction. Methods to achieve multi-focal imaging in scanning microscopy include time division multiplexing (TDM) and wavelength division multiplexing (WDM). A time division multiplexing technique [23] takes advantage of two sequences of excitation pulses with different wave-front divergence (thereby to focus on two different depth positions) interleaved in time. The signal generated at the two

depth positions can be de-multiplexed in time to realize bi-focal imaging. A wavelength division multiplexing technique, which is usually based on the chromatic aberration of some optics in the imaging system, focuses different wavelengths of a broadband source onto different axial positions inside a specimen. Light reflected from different axial positions has different wavelengths and therefore can be detected in parallel by using a spectrometer.

Here we propose a method for high-speed laser scanning microscopy. By utilizing an array of 45°-tilted micro mirrors arranged along the axial direction, fluorescence signals emitted from different axial positions of the specimen are orthogonally reflected and spatially separated on an image sensor for parallel detection, by which the more challenging axial imaging is converted to a lateral imaging problem. Within the micro mirror array (MMA), each micro mirror behaves effectively as a confocal pinhole with finite dimension placed at one certain axial position, providing optical sectioning capability. The technique significantly enhances the efficiency of axial imaging. Numerical analysis shows that nearly diffraction limited axial resolution can be achieved in the axial imaging. Photoresist-based micro mirror arrays are fabricated with photolithography and sputtering-coated with aluminum to enhance the reflectivity. Z-imaging of multiple microspheres located at different axial positions is experimentally demonstrated. We believe this technique can also be extended to various imaging modalities.

Wavefronts of emitters located at different axial positions can be de-multiplexed by using a micro-mirror array (MMA). Fig.2.2.1 illustrates its basic principle. Image signals generated in a specimen are focused onto an MMA, in which each micro-mirror is tilted at 45° with respect to the axial direction. Note that strong diffraction of a converging wave only happens near its focus, where effective interaction with the micro-mirror can occur. Consequently, each micro-mirror behaves effectively as a confocal pinhole, providing optical sectioning capability. After being reflected by the corresponding micro-mirrors and subsequently imaged by a lens, the image signals from different axial positions can be detected in parallel by using a detector array.

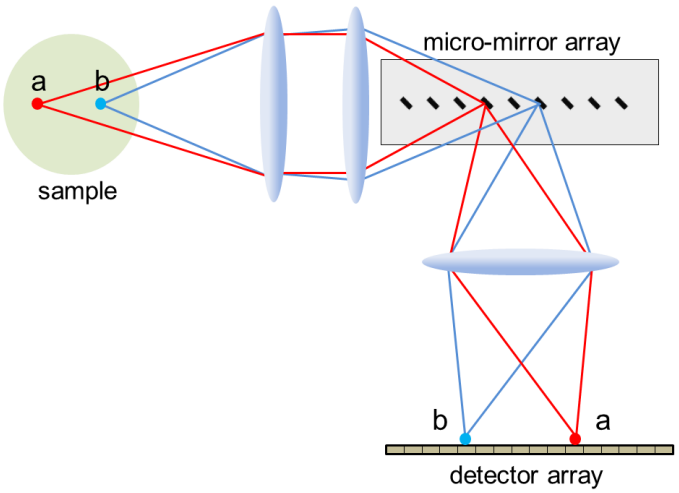

Figure 2.2.1Schematic diagram illustrating the principle of z-microscopy.

2.3 Numerical modeling and simulation of micro mirror array device

Before the actions of fabricating the micro mirror array device and building the actual imaging system, we carried out investigations on the diffraction of a converging wave by an array of micro mirrors. Under the paraxial approximation the axial intensity distribution near the focal point of a lens is given by $I(z) \propto \sin c^2(z \cdot NA^2 / 2\lambda)$ as shown in the upper curve of Fig. 2.3.1 (a), where NA denotes the numerical aperture of the focusing lens, λ is the wavelength, and z is the on-axis distance from the focal point. In our simulation, there is no loss of generality in assuming such a configuration that one of the mirrors named 'target mirror' is located at the peak position (focal point) while the rest are located at the null positions of the intensity distribution, corresponding to a mirror separation of $MS = 2\lambda / NA^2$ as depicted in Fig. 2.3.1 (a). The focusing lens is assumed to have numerical aperture $NA = 0.42$ and a wavelength of $\lambda = 410nm$ is used in our calculation. The micro mirrors are 45° tilted with respect to the z-axis and have parallelogram cross-section in the x-z plane (cf. Fig. 2.4.1 (b)). The width of each mirror MD is set to $0.61\lambda / NA$, which is one half of the size of the airy disk. The thickness of the micro mirror MT is chosen to be one half of its width (c.f., the inset of Fig. 2.3.1(a)). The field at the input plane shown in Fig. 2.3.1 (a) is given by

$$U_0(x,y) = \iint_{\sqrt{f_x^2+f_y^2} \le \frac{NA}{\lambda}} df_x df_y e^{i2\pi(f_x x + f_y y)} e^{-i2\pi L\sqrt{\left(\frac{1}{\lambda}\right)^2 - f_x^2 - f_y^2}} \quad (1)$$

,

which represents a converging wave focused in free space at a distance L from the input plane. The computational region of interest (ROI) is set to be the three-dimensional space between the dotted-line-marked input plane and the output plane located at the immediate end of the last mirror (50 μm × 50 μm × 46 μm). The ROI is then divided into 2000 slices along the z direction with a uniform step $\Delta z \sim 23$ *nm* and the FFT-based beam propagation method [24] is employed to simulate the diffraction of this focused beam by the array of ten micro mirrors with slanted square aperture. Regarding the detail of the algorithm, the propagation of the field from the $(n-1)^{th}$ plane to the n^{th} plane is governed by

$$U_n(x,y) = IFT\left\{ FT\left[U_{n-1}(x,y)\right] \times \exp\left(i2\pi\sqrt{\frac{1}{\lambda^2} - f_x^2 - f_y^2}\cdot \Delta z \right) \right\} \times P_n(x,y), \qquad (2)$$

where FT stands for the two-dimensional (2D) Fourier transform, IFT represents the 2D inverse Fourier transform, and $P_n(x,y)$ is the aperture function (equal to 1 in free space).

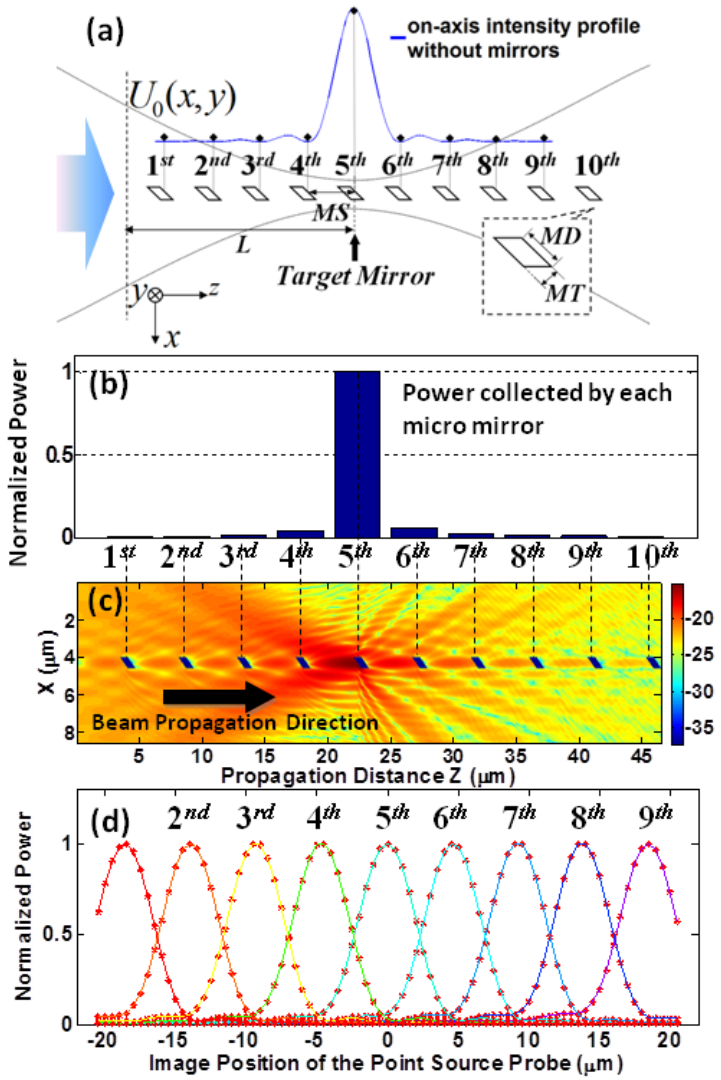

Figure 2.3.1 Numerical analysis of the system impulse response (a) Schematic diagram of the simulation model: a converging wave is diffracted by an array of ten micro mirrors; (b) Normalized power collected by each micro mirror when a converging beam is focused on the target mirror (i.e., the 5th micro mirror); (c) Intensity distribution (in logarithmic scale) in the x-z axial slice plane showing the diffraction of a converging beam by the micro mirror array; Strong diffraction occurs at the target mirror (5th mirror) where the beam is focused at; The reflected wave is not tracked in the calculation and assumed to be completely detected; (d) Simulated impulse response; The horizontal axis denotes the position at which the probe beam is focused (i.e., the geometric image position of the point source probe) while the vertical axis represents the normalized power detected by each detector; Each curve corresponds to the response of a different detector.

Each micro mirror is modeled as a staircase stack of rectangular apertures. The field fall inside the aperture is set to zero (i.e., assumed to be completely reflected off the beam propagation direction) and the power removed is accounted as part of the total detected power of the micro mirror. In our analysis, the reflected wave is not tracked and assumed to be completely detected by detectors. The calculated intensity distribution of the forward propagating beam in the x-z plane (at y=0) is shown in Fig.2.3.1(c) in the logarithmic scale. The power collected by each mirror (normalized to the power collected by the target mirror) is obtained and shown in the bar chart of Fig.2.3.1(b). The existence of crosstalk can reduce the bandwidth of the imaging system hence the axial spatial resolution. According to our simulation, the total power detected by non-target mirrors is less than 12%, which is low and is mainly contributed by the neighboring mirrors. To explore more details about axial resolution, we define the impulse response function of the system $h(n,z)$ describing the power emitted from a point-source probe at axial position z and detected by the n^{th} micro mirror that is located at axial position z_n. In the asymptotic case where the size of each micro mirror is much smaller than the wavelength, the diffraction effect is weak and we can assume that the axial intensity distribution is hardly perturbed by the mirrors. Under this assumption and the paraxial approximation, the impulse response function is given by $h(n,z) \propto \sin c^2(\frac{z-z_n}{2\lambda / NA^2})$, indicating that the system behaves as a low-pass triangular filter with a bandwidth $\sim NA^2 / 2\lambda$. According to

the Nyquist-Shannon sampling theorem, if the micro-mirror spacing, i.e., the sampling period, is smaller than half of the inverse of the bandwidth, reconstruction with diffraction limited axial resolution can be accomplished. Fig.2.3.1 (d) shows the simulated impulse response of the system with the ten micro mirrors. The horizontal axis denotes the position at which the probe beam is focused (i.e., the geometric image position of the point source probe) while the vertical axis represents the normalized power detected by each detector. Each curve corresponds to the response of a different detector. It can be seen that the full width at half maximum of each curve is approximately equal to the mirror spacing, i.e., $2\lambda / NA^2$. This numerical analysis therefore validates the proposed z-microscopy concept, and indicates that it can potentially achieve nearly diffraction limited axial resolution (e.g., $\sim 4\lambda / NA^2$ in the above example).

2.4 Experimental demonstration of the micro mirror array device

To experimentally demonstrate the principle of z-microscopy, we fabricated MMAs by using photolithography. We first spin coated hexamethyldisiloxane on a single-polished 4-inch (100) oriented silicon wafer to serve as the adhesive layer. A layer of KMPR 1010 (Micro Chem) negative photoresist was then spin coated and baked at 100 ℃ for 7 minutes. The height of the micro mirrors is determined by the thickness of the photoresist, which is controlled by adjusting the spinning speed. The wafer was then patterned by lithography, followed by 3 minutes' post-exposure

baking at 100 ℃. The sample was diced before development to minimize the shear stress that the micro mirrors would otherwise suffer. Each individual device was then developed with CD26 developer until no photoresist residual was observed. The developed device was then coated with 200-nm-thick aluminum in a sputtering system to enhance its reflectivity. Fig.2.4.1 (a) shows an optical micrograph of a fabricated MMA device. An array of micro mirrors standing on silicon substrate can be observed. A top-view and a close-view scanning electron microscope image is shown in Fig.2.4.1 (b) and (c), respectively. Each micro mirror has a dimension of 9.3μm (width) × 9.6μm (height) × 4.6 μm (thickness) and the separation between two neighboring mirror is 26.7 μm.

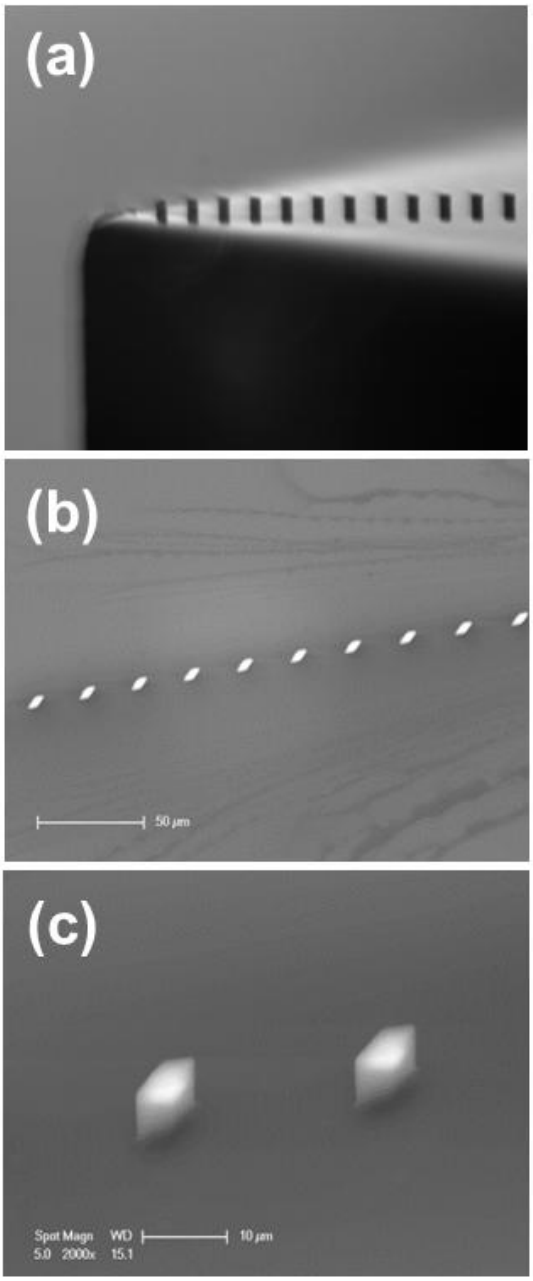

Figure 2.4.1 Fabricated micro mirror array; (a) Optical microscope image of an array of micro mirrors standing on a silicon substrate; (b) Top view microscope (NIKON L200ND) image of the micro mirror array. The mirrors are tilted by 45 ° with respect to the light incidence direction. (c) A scanning electron microscope (FEI Philips XL-20 SEM) image showing two adjacent micro mirrors.

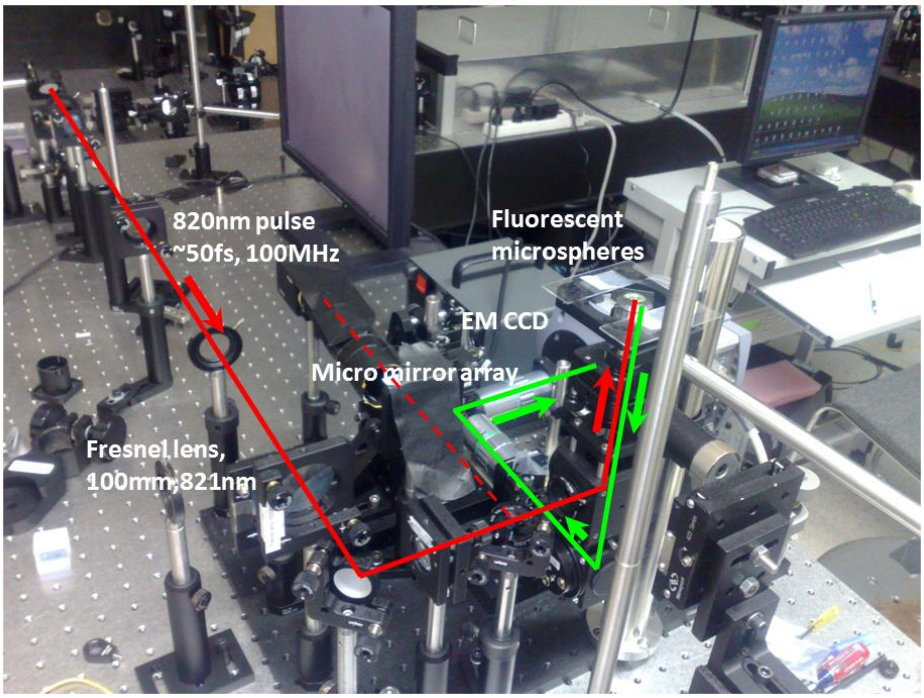

Figure 2.4.2 Picture showing the setup of the Z-microscopy experiment.

Fig.2.4.2 is a picture of the experimental setup. The laser output from a mode-locked femtosecond laser (KMLabs, $\lambda_c = 820nm$, Rep Rate ~100MHz, Pulse Width ~50fs) was expanded and focused with a Fresnel lens (design wavelength: $\lambda_0 = 821nm$, design focal length: $f_0 = 100mm$). Since the focal length f of a Fresnel lens depends on the wavelength λ and is given by the relation $\lambda f = \lambda_0 f_0$, different wavelengths of the femtosecond pulse were focused to different axial positions, resulting in a chromatically extended depth of focus. The beam is then re-collimated with a lens and focused onto specimen by an objective lens (100 ×, Carl Zeiss Jena, Apochromat HI100/1.32) to generate fluorescence within the scaled depth of focus via two-

photon excitation. The epi-detected fluorescence signal was collected by the same objective lens, filtered by a dichroic mirror and a band-pass filter, and focused onto the MMA by a long-working-distance objective lens (Mitutoyo 20× LWD). The fluorescence signal generated at different axial positions is therefore imaged onto the corresponding micro-mirrors (cf. Fig.2.4.3 (c)), and mapped to different horizontal positions on a charge-coupled-device (CCD) by another objective lens (Mitutoyo 50× LWD). In other words, the front-most Fresnel lens makes an on-axis 'ruler' by chromatically extending the pulse energy along axial direction. The following 4-F system (composed of a collimating lens and a 100× objective lens) scales down this 'ruler' and projects it onto the specimen to excite two-photon fluorescence. The effective imaging depth range Δz is determined by Eq.2.4.1 [25]

$$\Delta z = \frac{|\Delta\lambda|}{\lambda_0} f_0 \frac{1}{n_{oil}} \left(\frac{f_{OL}}{f_2} \right)^2 = \frac{|\Delta\lambda|}{\lambda_0} f_0 n_{oil} \left(\frac{NA_2}{NA_{OL}} \right)^2 = \frac{|\Delta\lambda|}{\lambda_0} f_0 n_{oil} \left(\frac{NA_{FL}}{NA_{OL}} \right)^2, \quad (2.4.1)$$

where $\Delta\lambda$ is the spectral bandwidth of the excitation beam, f_0, f_{OL} and f_2 are the focal lengths of the Fresnel lens, the focusing objective lens and the collimating lens right after the Fresnel lens. n_{oil} is the refractive index of the optical index oil. λ_0 is the design wavelength of the Fresnel lens. To acquire the fluorescence signal, the same 100× objective lens and a long-working-distance objective lens (Mitutoyo 20× LWD) compose another 4-F system and map the fluorescence onto the MMA to horizontally image the axial distribution of the fluorescence signal.

In order to calibrate the relationship between the sample depth and the number of target mirror, which is the depth response of our imaging system, a single fluorescent microsphere with 2μm diameter is scanned along axial (z) direction with 0.5μm step size. A sequence of line images obtained at a series of axial positions is shown in Fig.2.4.3 (d). The depth-mirror mapping relationship can then be obtained as depicted in Fig.2.4.3 (e). The calibration curve of the depth response can be fitted linearly with a slope of 3.3μm/mirror number, indicating an effective axial separation of about 3.3 μm in the sample space between two adjacent micro mirrors.

In order to demonstrate the z-imaging capability, the system is used to image multiple 10μm-diameter fluorescent microspheres located at different axial depths in the sample space. Fig.2.4.4 (a) is the microscopic image of multiple fluorescence microspheres to be imaged. Please be noted that they are not located on one single lateral plane and especially one microsphere (pointed by red arrow) with obvious out-of-focus imaging effect is very different from all others in depth. Artistic schematic (Ref. Fig.2.4.4 (b)) shows the distribution of these microspheres. XY cross sectional images at four axial planes indicated in Fig.2.4.4 (b) from bottom to top are corresponding with images of Fig.2.4.4 (c, d, e, f), individually. The four axial images have adjacent separation of ~ 3.3 μm and are acquired simultaneously by four adjacent micro mirrors of an MMA. Microspheres at different depths are resolved. Compared with the wide-field image (cf. Fig.2.4.4 (a)) the out of focus fluorescence signal in Fig.2.4.4 (f) is significantly suppressed, demonstrating the optical

sectioning ability of the imaging system.

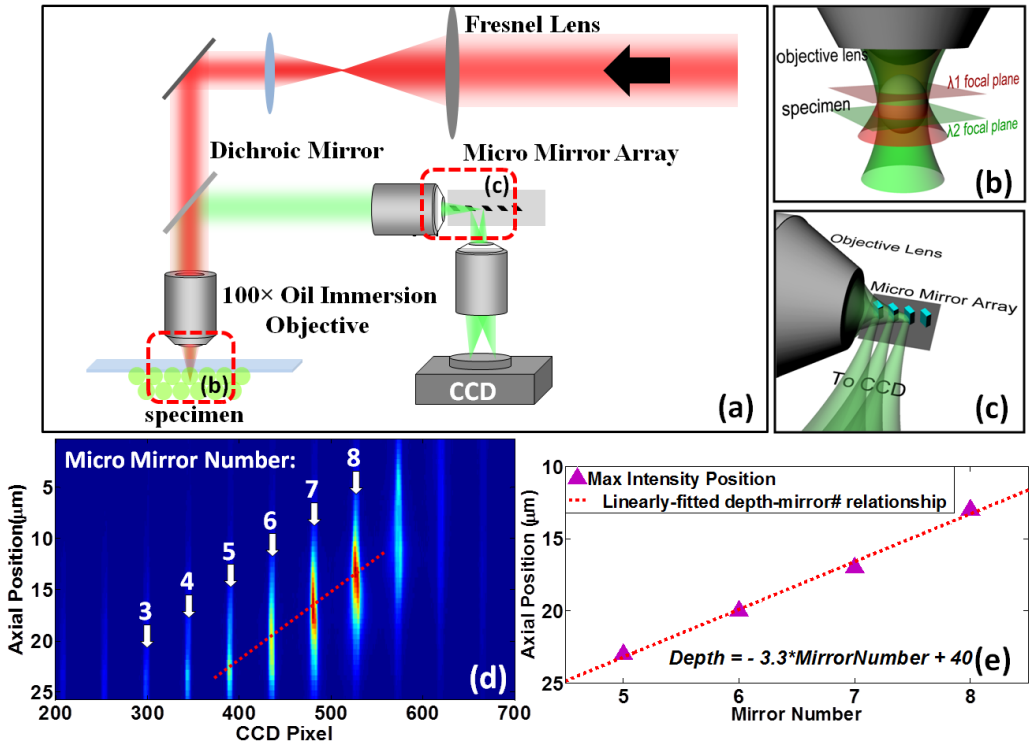

Figure 2.4.3 (a) Schematic diagram of the experimental setup; (b) Chromatically extended depth of focus; Different wavelengths of the excitation pulse are focused to different axial positions due to purposely introduced chromatic aberration; (c) Z-imaging by using a micro mirror array; Micro mirrors are tilted at 45 ° with respect to the axial direction to de-multiplex fluorescence signals excited at different axial positions for parallel detection. (d) Depth response measured by scanning a 2-μm fluorescent microsphere along the axial direction; Each row of the figure is a line image acquired when the microsphere probe was at an axial position specified by the vertical axis; (e) Calibrated depth position – mirror number mapping relationship, indicating an effective axial separation of about 3.3 μm in the sample space between two adjacent micro mirrors.

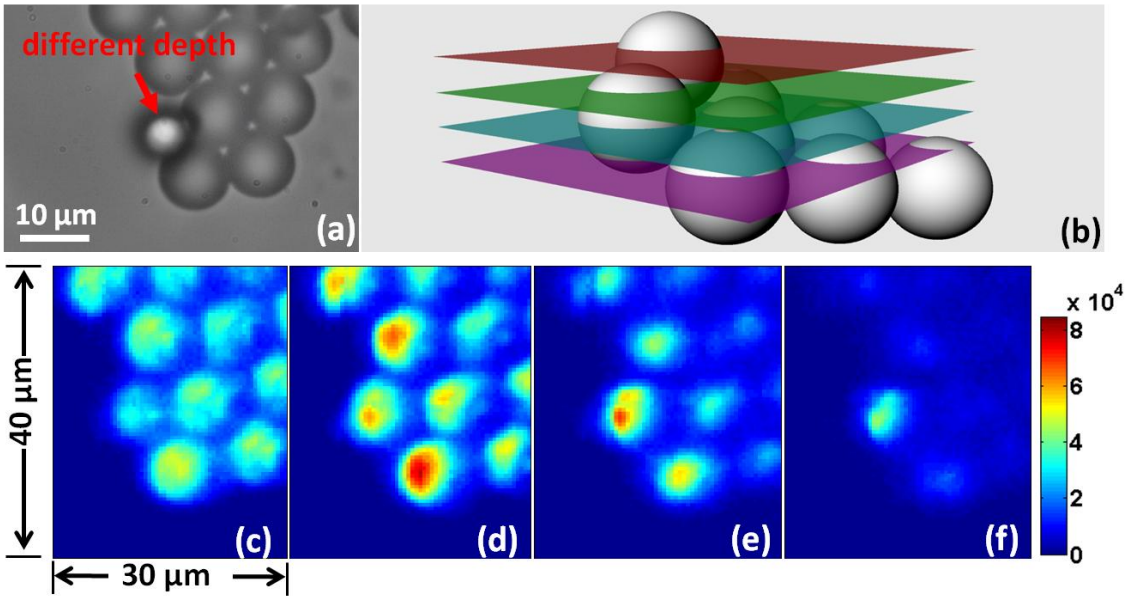

Figure 2.4.4 Z-imaging experimental results (a) Micrograph of the sample (i.e., multiple microspheres) used in the experiment; One microsphere is located at a very different depth level; (b) Artistic schematic showing multiple axial planes simultaneously imaged by the micro mirror array; (c)-(f): Imaging results at four axial positions obtained by using the micro mirror array; Microspheres at different depths are resolved; The optical sectioning ability of the imaging system can be clearly observed as the out-of-focus fluorescence signal is significantly suppressed [see (a) and (f)].

In section 2.2 – 2.4, our numerical analysis and experimental demonstrations are mainly focused on two-photon fluorescence imaging. However, this technique can also be extended to other imaging modalities like confocal fluorescence microscopy, and therefore could be useful in many more applications.

2.5 Introduction to second-harmonic imaging microscopy

Second harmonic generation (SHG) is a second-order nonlinear optical process in which two photons of same frequency are combined in some nonlinear material with a noncentrosymmetric molecular structure and hence non-vanishing

$\chi^{(2)}$ to generate a new photon with twice the energy. SHG is different from two-photon excitation process for the fact that SHG is a coherent process, not related to any absorptive process. Usually, nonlinear polarization of the medium is induced by a focused intense laser field. This process is also confined to the focal center of the excitation beam waist. The resulted emission is a coherent wave at exactly twice the incident frequency. The magnitude of the SHG response can be enhanced by optimizing the phase matching conditions.

Second harmonic generation was first demonstrated in University of Michigan in 1961 with a quartz sample [26] after the invention of laser. In 1977, Colin Sheppard combined SHG method with a scanning optical microscopy to acquire images of various nonlinear crystals [4]. Based on SHG, the technique of second-harmonic imaging microscopy was developed as an imaging contrast mechanism for investigating the structure and functions of various biological specimen including cell and tissue. There are several obvious advantages attached to this imaging modality. The process of second harmonic generation doesn't involve the excitation of molecules, and therefore the photodamage to biological samples can be minimized. Also, by using incident light at NIR wavelengths, the deep penetration depth enables three-dimensional imaging of thick tissues.

2.6 Chromatic SHG for non-axial scanning 3D imaging

SHG imaging utilizes the second order nonlinear susceptibility $\chi^{(2)}$ as an imaging contrast mechanism. This modality could be applied to the imaging of samples with second-order nonlinearity, or the surfaces of specimens with inversion symmetry in which $\chi^{(2)}$ vanishes in the bulk under electric dipole approximation [27].

Laser-scanning second harmonic generation (SHG) imaging [28-32] combines SHG method and laser-scanning mechanism to reconstruct the three-dimensional image of specimen. As an emerging nonlinear optical imaging modality, it has been extensively investigated in recent years.

Despite all significant advantages already mentioned in Section 2.5, conventional SHG imaging requires three-dimensional (3D) point-by-point scanning, which can significantly limit the 3D or the x-z and y-z (x, y: lateral directions; z: axial direction) cross-section imaging speed. To address this challenge, here we explore a chromatic SHG imaging technique, which can eliminate mechanical axial scanning by exploiting the chromatic aberration of the Fresnel lens.

The chromatic scanning technique was previously applied to epi-reflection confocal microscopy [33-36]. Our group has recently extended it to two-photon

fluorescence imaging [25, 37]. For example, in my project of Z-microscopy fluorescence imaging described in Section 2.2-2.4, similar technique was exploited.

To illustrate the underlying principle, let us consider focusing a pulsed fundamental beam by a Fresnel lens. As previously mentioned in section 2.4, the focal length f of the Fresnel lens is a function of wavelength and satisfies the relationship $\lambda f = \lambda_0 f_0$ [38, 39], where the λ_0 and f_0 stand for design wavelength and the corresponding design focal length. Consequently, the different wavelength components of the incoming pulse are focused to different axial positions with the shorter wavelength further away from the Fresnel lens. Axial scanning is therefore effectively realized through the chromatic aberration of the Fresnel lens. The focused and chromatically aberrated beam can then be relayed through imaging optics to achieve desired lateral and axial resolutions, and produce second harmonic signal if interacting with a specimen of interest with a non-vanishing $\chi^{(2)}$. Notice that the SHG signals at different axial positions are generated by different fundamental wavelengths and as a result must have accordingly different wavelengths. A spectroscopic measurement can then resolve the signals (or raw pixel values) generated at different axial positions. In other words, axial imaging can be achieved in parallel without mechanical axial scanning, and 3D images can be obtained by scanning the chromatically aberrated fundamental beam (or the specimen) only in two lateral directions. It should be noted that there is a trade-off between the

chromatic scanning range and the required pulse energy. In general, the larger the chromatic aberration the more pulse energy is needed to yield the same signal strength.

The schematic diagram of our experimental setup is shown in Fig.2.6.1. It is similar to that used in my prior chromatic two-photon imaging work. Briefly, femtosecond laser pulses from a Ti: sapphire mode-locked laser (KMLabs, pulse width ~50 fs, repetition rate ~100 MHz, center wavelength ~820 nm) were delivered to our experimental system through a 40-cm-long photonic crystal fiber (Thorlabs, ESM-12-01). The fiber output was collimated by an objective (20×, NA 0.4) and subsequently expanded with an imaging system consisting of two lenses with focal lengths of 75.6 mm and 250 mm respectively. A Fresnel lens (design wavelength: λ_0 = 821 nm, design focal length: f_0 = 100 mm) was then utilized to focus the beam.

As aforementioned, due to the chromatic aberration, different wavelengths of the laser beam were focused to different axial positions, effectively realizing axial scanning. To achieve desired axial and lateral resolutions, the beam was re-collimated by a lens (focal length: 38.1 mm), reflected by a dichroic mirror (Thorlabs DMLP505), and focused by an objective lens (60×, NA 0.85) onto a sample. The second harmonic signal generated in the sample was then collected in the forward direction by another objective lens (20×, NA 0.4). After passing through a band-pass filter (Chroma Tech., 405/40BP), which was used to eliminate the fundamental beam,

the second harmonic signal was coupled into a five-meter-long multimode fiber. Finally, the output signal from the multimode fiber was detected by a spectrometer (PI/Acton SpectraPro 2500 with a liquid nitrogen cooled charge coupled device detector PI/Acton Spec-10).

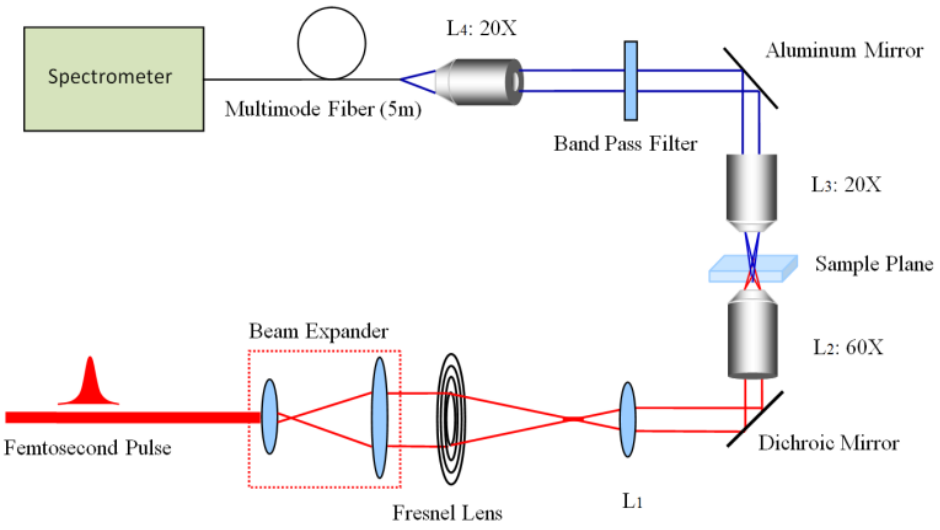

Figure 2.6.1 Schematic diagram of the chromatic second harmonic imaging system.

We characterized the effective chromatic scanning range of the system. To this end, we air-dried a thin layer of $BaTiO_3$ nanocrystal (Nanostructured & Amorphous Materials Inc., Average Particle Size: 200nm, Morphology: Spherical) solution (suspended in water) on a microscope cover slide (VWR Micro Cover Glass). A single cluster of nanocrystals (c.f., the microscope image shown in Fig.2.6.2 inset) was identified and placed near the focal plane of the objective lens L_2 (c.f., Fig.2.6.1) as a second harmonic probe. The cover glass and hence the

nanocrystal cluster was scanned vertically by using a computer-controlled motorized translational stage. The generated second harmonic signal was then collected and coupled into a five-meter-long multimode fiber, and detected by the spectrometer. Fig.2.6.2 shows our measured results. Each row of the figure represents a spectrum of the second harmonic signal generated by the $BaTiO_3$ nanocrystal cluster placed at a corresponding axial position as indicated in the vertical axis. As the nanocrystal was moved away from the objective, the center wavelength of the second harmonic signal shifted towards shorter wavelength, as expected from the focal length-wavelength relation of the Fresnel lens. This clearly demonstrates the chromatic scanning behavior. An effective chromatic scanning range of about 8 μm in the sample plane is obtained. For each wavelength, we found the corresponding depth position that yielded the maximum second harmonic signal (i.e., where the fundamental wavelength is focused). The obtained depth position (z)-wavelength (λ) relationship is shown in Fig.2.6.2 (b), which can be fitted with a linear curve with a slope of about 1.1 μm/nm.

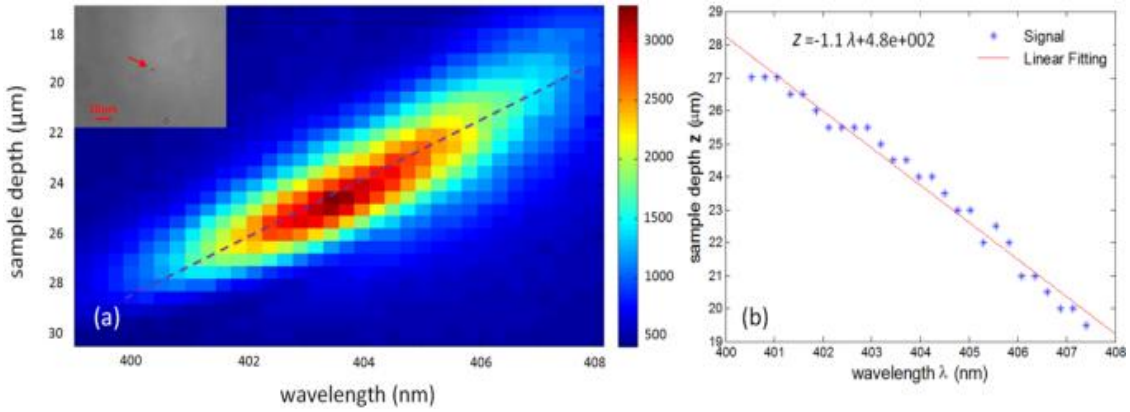

Figure 2.6.2 (a) Second harmonic spectrum generated at different depth positions; A single cluster of nanocrystals (shown in the upper-left inset) was placed near the focal point of the objective lens L_2 (c.f. Fig. 1). A sequence of spectra of the generated second harmonic signal was measured as the nanocrystal cluster was mechanically scanned. (b) Mapping relationship between the depth position and the second harmonic signal wavelength; in the equation, λ represents the signal wavelength in nm while z is the depth position in μm.

To demonstrate the chromatic imaging capability, we utilized our system to image the surface of a $LiNbO_3$ crystal, which was purposely scratched by silicon carbide sandpaper. An optical microscope image of the crystal is shown in Fig.2.6.3 (a), in which the region of interest (30 μm × 30 μm) is overlaid with a pseudo-color SHG image. Two-dimensional point-by-point lateral scanning of the crystal sample was performed with a scanning step of 1 μm by using computer-controlled translational stages (Newport ESP300 3-Axis Motion Controller with motorized actuator). At each point a second harmonic spectrum was recorded, from which the axial image information is obtained. Fig.2.6.3 (b) shows a series of second harmonic images at wavelengths from 404 nm to 413 nm with an interval of 0.52 nm. The "X' shaped grooves on the crystal surface can be observed. The vertical cross section of

the grooves can be better visualized in Fig.2.6.3 (c), in which the $x-\lambda(z)$ cross-section images at three different positions (i.e., y = 20 μm, 26 μm, and 30 μm respectively) are shown. It appears that the grooves are tilted with respect to the crystal surface, which is not unexpected considering that the surface was randomly scratched.

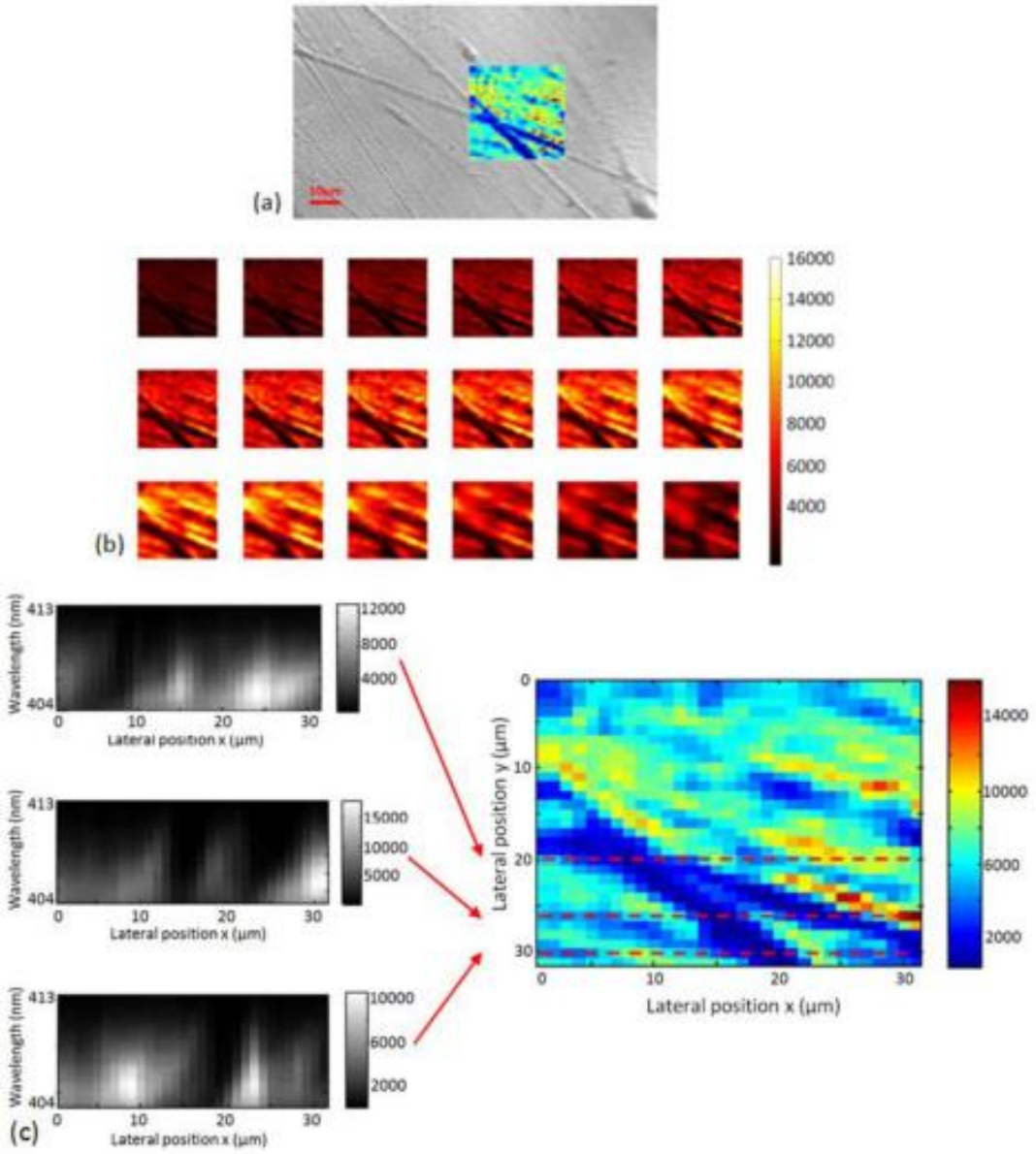

Figure 2.6.3 (a) Microscope image of a LiNbO3 crystal scratched by silicon carbide sandpaper showing an "X" shaped scratch on its surface (b) Chromatic second harmonic imaging results; the crystal was scanned in two lateral dimensions (30 μm × 30 μm). A series of second harmonic images at wavelengths from 404 nm to 413 nm with an interval of 0.52 nm were obtained and shown here. (c) Side cross-sectional imaging results; three images correspond to y = 20 μm, 26 μm, and 30 μm respectively.

In addition, we also imaged a $LiNbO_3$ microcrystal created by using the same scratching method. A microscope image of the microcrystal is shown in Fig.2.6.4 (a). Similarly, a two-dimensional lateral scan of the sample over an area of 40 μm × 40 μm was performed. The obtained SHG images at wavelengths from 404.2 nm to 410.0 nm with an interval of 0.52 nm is shown in Fig.2.6.3 (b). Fig.2.6.3 (c) shows three $x-\lambda(z)$ cross-section images at y = 10 μm, 26 μm, and 28 μm respectively. Although due to the limited axial scanning range and spatial resolutions the quality of these images needs further improvement, these preliminary proof-of-concept results have clearly demonstrated the 3D imaging capability of the chromatic SHG technique.

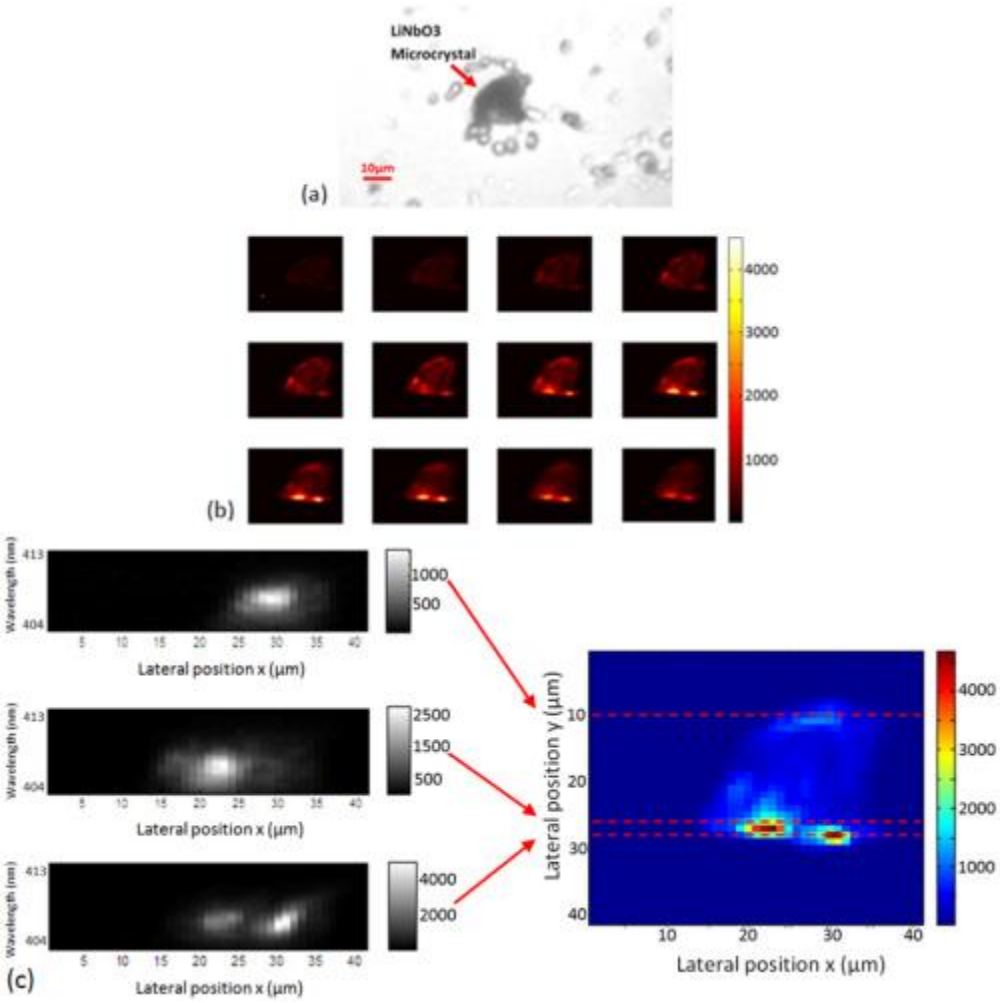

Figure 2.6.4 (a) Microscope image of a LiNbO3 micro-crystal; (b) Chromatic second harmonic imaging results; the sample was scanned in two lateral dimensions (40 μm × 40 μm). The second harmonic images correspond to wavelengths from 404.2 nm to 410.0nm with a step of 0.52 nm; (c) Side cross-sectional imaging results; three images correspond to y = 10 μm, 26 μm, and 28 μm respectively,

In the current work, a multimode fiber was used to collect the SHG signal and deliver it to the spectrometer. Since the second harmonic beam had large chromatic aberration and hence was launched into multiple spatial modes, significant amount of signal power was lost when coupled through the entrance slit of the

spectrometer. To improve the overall SHG signal collection efficiency, here we propose a method to collimate the chromatically aberrated second harmonic beam by using chromatic material dispersion. Qualitatively, a shorter-wavelength SHG signal (corresponding to a shorter fundamental wavelength) is nearer to the collecting lens, which implies that the chromatic aberration of the collecting lens should be opposite to that of the Fresnel lens in order to collimate the second harmonic beam. Note that for a singlet lens, the focal length f is given by $1/f = (n-1)(1/R_1 - 1/R_2)$ [40] where n is refractive index and R_1 and R_2 are the radius of curvatures of the two facets. For lens material with normal dispersion, the shorter the wavelength the larger the index of refraction is (hence a shorter focal length). Therefore, chromatic material dispersion can compensate for the chromatic aberration produced by the Fresnel lens and result in a better-collimated second harmonic beam. Fig.2.6.5 (a) shows a schematic diagram of such a chromatic SHG imaging system with improved collection efficiency. For simplicity we assume that lenses L_1 and L_4 are achromatic and have the same focal length, and so do lens L_2 and L_3 (c.f. Fig.2.6.5 (a)). Note that the change of focal length of the Fresnel lens as a function of wavelength satisfies

$$\frac{\Delta F}{F} = -\frac{\Delta \lambda_f}{\lambda_0} = -\frac{\Delta \lambda_{SHG}}{\lambda_0 / 2} = -\frac{\Delta \lambda_{SHG}}{\lambda_{SHG}} \qquad (2.6.1)$$

Where λ_0 is the design wavelength (at fundamental frequency), and the subscript f and SHG stand for the fundamental and SHG wavelength respectively. On the other

hand, for a singlet lens the change of focal length as a function of wavelength satisfies

$$\frac{\Delta f}{f} = -\frac{\Delta n}{(n-1)} \quad (2.6.2)$$

To compensate for the chromatic aberration produced by the Fresnel lens, we require $\Delta F \approx -\Delta f$, which leads to

$$\frac{f}{F}\frac{\Delta n}{(n-1)} \approx -\frac{\Delta \lambda_{SHG}}{\lambda_{SHG}} \quad (2.6.3)$$

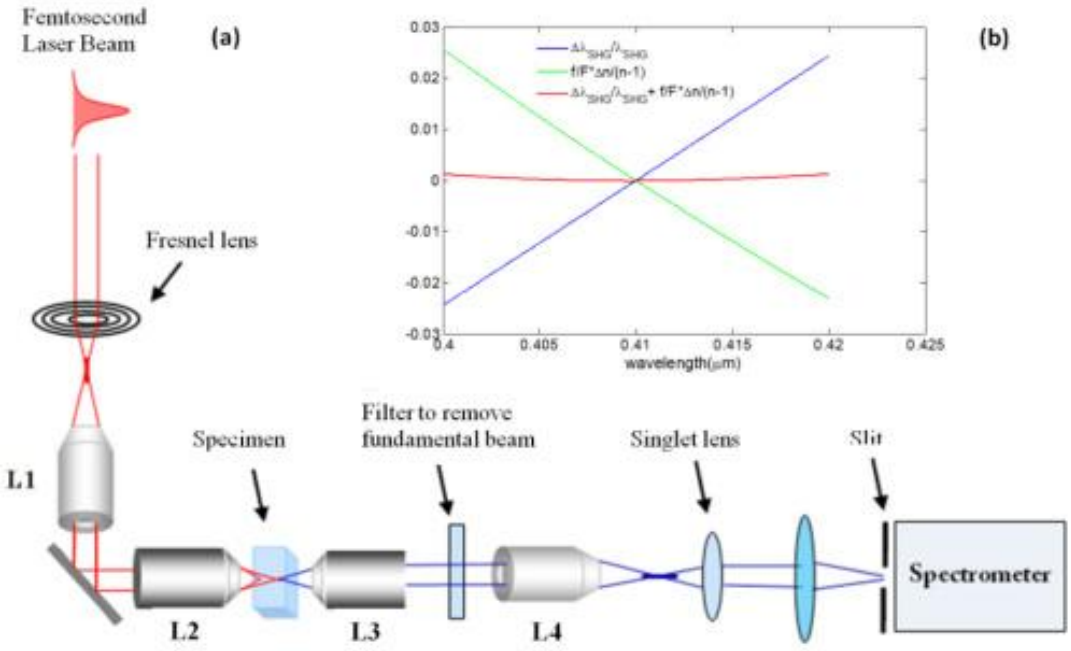

Figure 2.6.5 (a) Schematic diagram of a chromatic SHG microscope with an improved signal collection efficiency (b) an example showing that the material dispersion of a singlet lens (Material: N-SF11 glass, f/F = 3.37) can potentially help improve the SHG signal collection efficiently; the blue curve shows negative of the term on the right hand side of Eq. 2.6.3 is a function of the second harmonic wavelength while the green curve shows the term on the left hand side of Eq. 2.6.3; the red curve shows the sum of the two.

The chromatic aberration can be largely compensated in the example shown in Fig.2.6.5 if the lens material is N-SF11 glass and a ratio f/F = 3.37 is chosen. One can also use other highly dispersive lens materials and adjust the focal lengths of the two pairs of objectives to optimize the system design.

In summary, we have investigated the feasibility of chromatic second harmonic imaging, in which mechanical axial scanning is eliminated by utilizing the chromatic aberration caused by a Fresnel lens. In our proof-of-concept experiment, an approximately 8μm effective chromatic scanning range (measured in the air) has been achieved. It should be noted that the chromatic scanning range inside a medium differs from that in the air. One can utilize a second harmonic probe buried inside the medium to directly calibrate the system or calculate it from the wavelength-depth mapping relationship measured in the air (e.g., the scanning range in the medium is scaled by the average refractive index). We believe that this new technique has the potential to significantly improve the speed of SHG imaging and therefore useful for real-time applications such as monitoring dynamic biological processes in three dimensions.

CHAPTER 3. HOLOGRAPHIC COLLINEAR FROG FOR SPATIOTEMPORAL CHARACTERIZATION OF ULTRASHORT LASER PULSE

3.1 Introduction to femtosecond Ti: sapphire laser

Laser (Light Amplification by Stimulated Emission of Radiation), with its countless important applications in many aspects of human activities through the past half century since it was born, has been one of the greatest inventions in the human history. In 1917, Albert Einstein published the paper "On the Quantum Theory of Radiation" [41] to start establishing the theoretical foundations of the laser. In the following decades, several scientists contributed to the development of the idea, and eventually, in the year of 1960, Theodore H. Maiman at Hughes Research Laboratories used flashlamp to pump the ruby crystal to produce red laser light at 694 nm wavelength [42]. This is considered to be the first successful laser in the world. The discovery of ruby laser triggered strong curiosity to search for similar gain materials, and laser action in other solids, liquids, gases and semiconductors are demonstrated in succession. In the mid-1980s, Ti: sapphire laser was discovered as the most import tunable laser with tuning range 660 nm – 980 nm. In the late 1980s, people combined Ti: sapphire laser with ultrafast techniques including famous Kerr lens mode-locking to achieve mode-locked laser with pulse widths on the order of femtoseconds. Since the Ti: sapphire, as a laser gain media, has much broader gain

bandwidth comparing to rare-earth-doped gain medium, it can produce much shorter pulse.

My Ph.D. research projects are mainly based on the femtosecond Ti: sapphire laser systems (KMLabs) as shown in the Fig.3.1.1. The Ti: sapphire crystal is pumped by a diode-pumped solid-state (DPSS) 532 nm continuous-wave (CW) green laser (Coherent Verdi-V5). The pump beam with an average power of 4.5W is focused onto the Ti: sapphire crystal with Brewster angle of incidence. Kerr lens effect due to the strong electric field inside the nonlinear Ti: sapphire crystal is the mechanism for mode locking. A pair of cavity mirrors has high reflectance through a broad spectral range covering the fluorescent bandwidth of the gain media. A pair of prism is used to compensate for the dispersion introduced by the pulse propagation within the oscillator. A folded broadband mirror is exploited to reduce the footprint of the system.

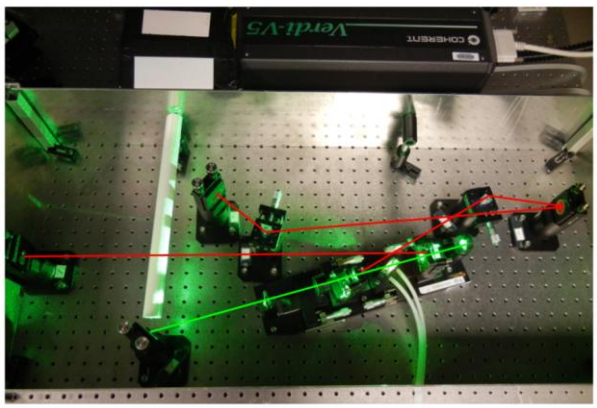

Figure 3.1.1 Femtosecond Ti: sapphire laser system

Typically, with 4.5W pump power, the output of the oscillator is around 820 nm with repetition rate at ~ 85 MHz. The average output power is ~ 400 mW. The pulse duration is ~ 50 fs at full width half maximum (FWHM).

Mode-locked femtosecond lasers have broad applications in varies fields of scientific research and industrial manufacturing. For example, in modern nonlinear optical imaging microscopy, due to the extremely high photon density required for critical nonlinear optical process to happen, femtosecond laser that can provide with ultra-high intensity within the pulse duration is necessary.

Along with the fast development of femtosecond laser technologies, the efforts to improve techniques for laser pulse characterizations have never been discontinued because of its crucial role in the development of laser and its applications. First of all, pulse characterization is a direct and efficient approach for the inspection and troubleshooting of a laser system. Second, for laser application engineers and scientists, information of pulse width and phase is demanded for their application solutions. Take two-photon imaging of deep tissue as an example, some negative dispersion needs to be introduced beforehand to compensate for the positive dispersion of the optics that pulse goes through before reaching the imaging spot [43 - 45]. In another example, the two-photon transition process can be controlled by purposely tailoring femtosecond laser pulses [46]. In the following sections, I will focus on the techniques for ultrafast pulse characterizations.

3.2 Methods for ultrashort pulse characterization

Autocorrelation is well known as a powerful tool for identifying fundamental frequency of a signal. In optics, through flexible configurations of experimental setup, various autocorrelation functions can be realized. Among which the most widely exploited are field autocorrelation, intensity autocorrelation and interferometric autocorrelation. Due to the limit of the slow response time of photodiodes and the much shorter pulse duration achieved through modern technologies, optical autocorrelation has been an irreplaceable approach for measuring ultrashort laser pulse.

As a simple and quick check on the duration of a femtosecond laser pulse, intensity autocorrelation has the most straightforward experimental setup as shown in Fig.3.2.1. Two copies of the pulse with different incident angles are focused onto a same spot inside a second-order nonlinear crystal like Barium borate (BBO).

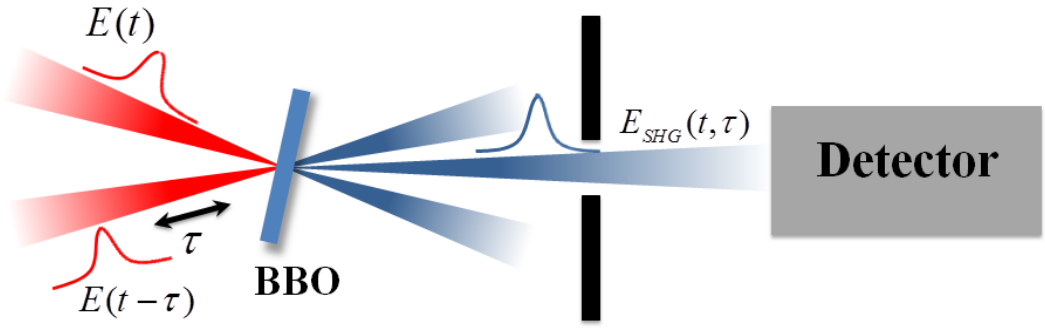

Figure 3.2.1 Illustrative diagram of experimental setup of optical intensity autocorrelation.

Given that the phase matching conditions are fulfilled by properly tuning the incident angles and the orientation of the crystal, the detected signal described by the equation $I(\tau) = \left|E_{SHG}(t,\tau)\right|^2 = \int_{-\infty}^{+\infty} I(t)I(t-\tau)dt$ is plotted versus the time delay τ between the two copies of the pulse. Fig.3.2.2 shows the simulation of the intensity autocorrelation of a perfect Gaussian pulse $E(t) = e^{-(\frac{t}{\tau_G})^2} e^{-j\omega_0 t}$, assuming $\tau_G = 50\,fs$ and the pulse spectrum is centered at 800 nm.

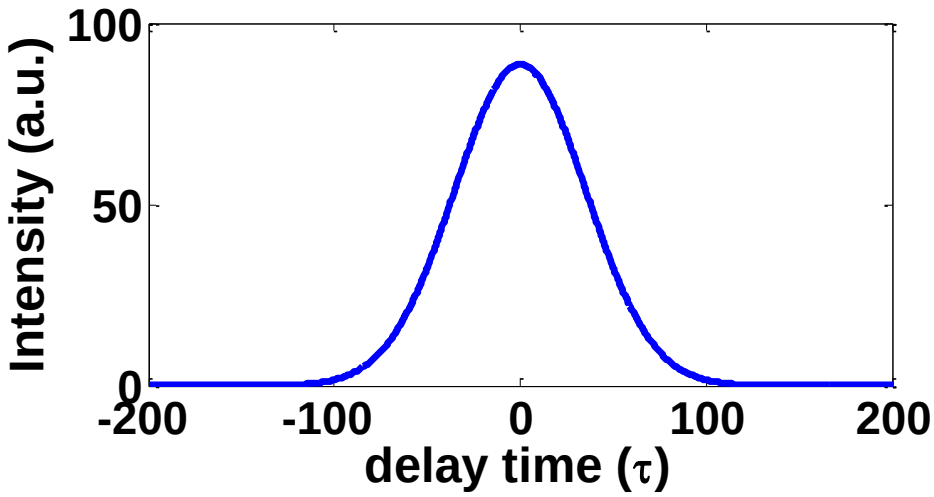

Figure 3.2.2 Simulated intensity autocorrelation of a Gaussian pulse with 50 fs pulse width and spectrum centered at 800 nm.

By analyzing the intensity autocorrelation data, information about the pulse duration could be extracted given that the type of pulse shape is known in advance, otherwise the pulse shape has to be assumed. For most cases, because of the varying experimental conditions and complex optical components involved, it is difficult to predict the pulse shape at a downstream path of the setup in advance.

Currently the most straightforward method for pulse characterization is interferometric autocorrelation. As shown in the illustrative diagram in Fig. 3.2.3, it is comparatively easy to align to the collinear configuration. Mathematically, the interferometric autocorrelation could be described by $I(\tau)=\int_{-\infty}^{+\infty}\left|[E(t)+E(t-\tau)]^2\right|^2 dt$. Fig. 3.2.4 shows the simulated interferometric autocorrelation of the same Gaussian pulse $E(t)=e^{-(\frac{t}{\tau_G})^2}e^{-j\omega_0 t}$ and the Fig. 3.2.5 is the trace shown on an oscilloscope in a real experimental setup.

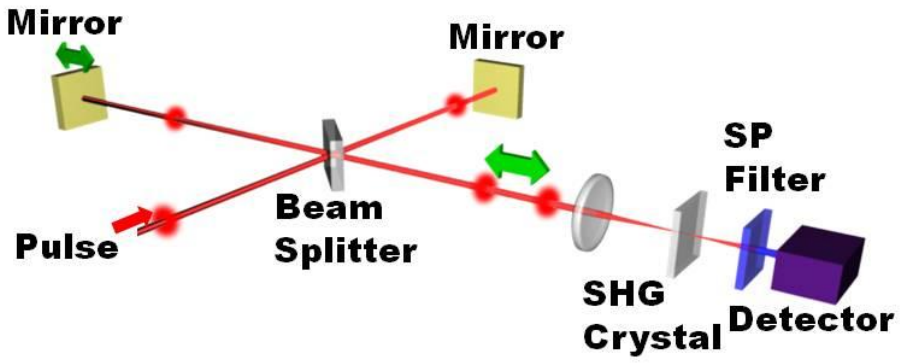

Figure 3.2.3 Illustrative diagram of experimental setup of interferometric autocorrelation (modified based on a figure from Wikipedia).

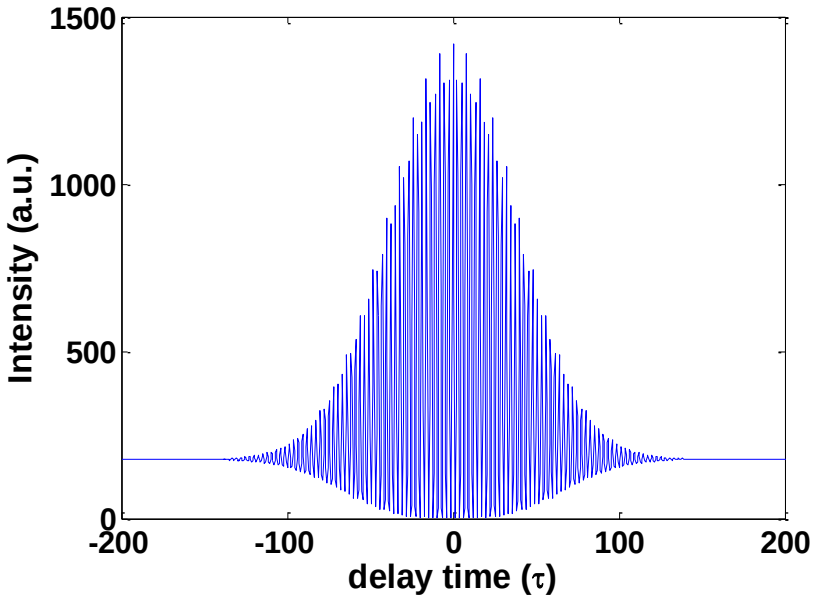

Figure 3.2.4 Simulated interferometric autocorrelation of a Gaussian pulse with pulse width 50 fs and spectrum centered at 800 nm.

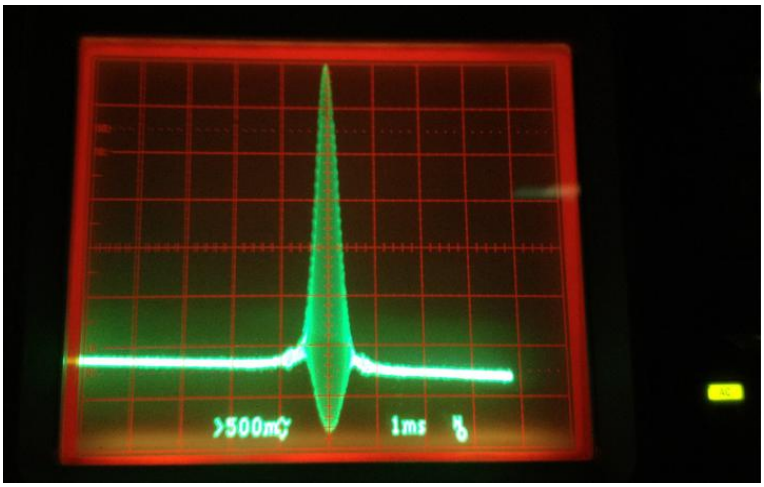

Figure 3.2.5 Two-photon-absorption based interferometric autocorrelation trace shown on an oscilloscope during experiment.

Actually the DC component of the interferometric autocorrelation trace, extracted through the method of Fourier transform, is the intensity autocorrelation of

the pulse. So the interferometric autocorrelation contains all the information an intensity autocorrelation could provide. Besides, when the pulse has chirp, carrier fringes at both wings of the central peak tend to be washed out, enabling the observation of chirping conditions of a femtosecond pulse through the method of interferometric autocorrelation.

With the development of ultrafast laser technologies, more advanced technologies for laser pulse characterization with better resolution and accuracy are invented. In 1991, Rick Trebino invented frequency-resolved optical gating (FROG) method [13, 14] for characterizing ultrashort laser pulse ranges from sub-femtosecond to nanosecond in length. Marcos Dantus at Michigan State University developed the approach of multiphoton intrapulse interference phase scan (MIIPS) [47, 48]. In 1998, Chris Iaconis and Ian Walmsley developed technique of spectral phase interferometry for direct electric-field reconstruction (SPIDER) [49 - 52].

Throughout the following sections of this chapter, my research work is basically based on the approach of frequency-resolved optical gating.

3.3 Introduction to Frequency-resolved optical gating (FROG) for pulse characterization

The ultrafast laser pulse is the shortest events ever created by human. It has been a common sense that in order to measure the time duration of an event, some

shorter event is required as the tool. Before the invention of FROG, it was difficult to measure the profile and phase of ultrafast laser pulses.

In 1991, Rick Trebino *et al* solved the problem [13, 14] by gating the pulse with itself in a nonlinear optical medium (doubling crystal) with the resulted signal resolved spectrally by a spectrometer. The spectrum is recorded as a function of delay between the two copies of the pulse. Thus a two-dimension pattern called FROG trace can be acquired in the $\omega - \tau$ domain. Its projection onto the delay axis τ gives the classical autocorrelation. By employing a two-dimension phase-retrieval algorithm, both the amplitude and the phase of the incident laser field can be revealed.

Take the most commonly used SHG-FROG as an example, the second-harmonic signal beam $E_{sig}^{SHG}(t,\tau) = E(t)E(t-\tau)$ is actually the same signal beam of the intensity autocorrelation described in the previous section. The only difference is that now the signal is spectrally resolved by a spectrometer. By scanning the delay τ between the two pulses, the resulting two-dimension trace can be written as Eq. 3.3.1 [53].

$$I_{FROG}^{SHG}(\omega,\tau) = \left| \int_{-\infty}^{+\infty} E_{sig}(t,\tau)\exp(-i\omega t)dt \right|^2 = \left| \int_{-\infty}^{+\infty} E(t)E(t-\tau)\exp(-i\omega t)dt \right|^2 \quad (3.3.1)$$

Figure 3.3.1 shows the simulated conventional SHG-FROG trace constructed from a Gaussian pulse $E(t) = e^{-(\frac{t}{\tau_G})^2} e^{-j\omega_0 t}$ with $\tau_G = 50\,fs$ and spectrum centered at 800 nm.

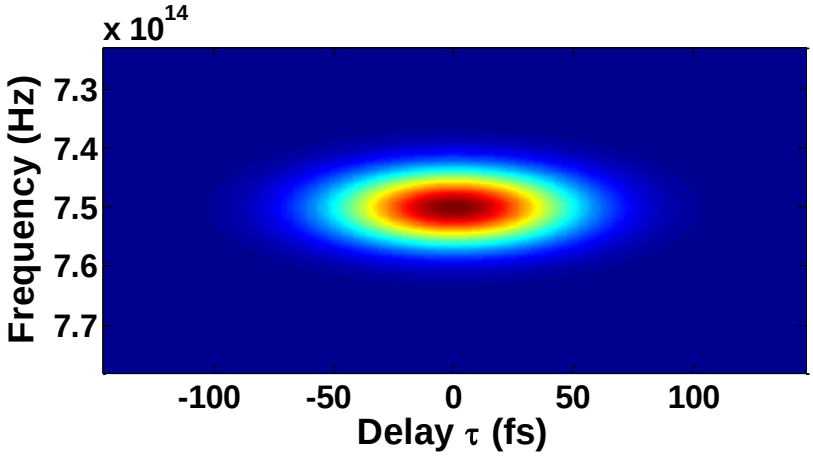

Figure 3.3.1 Simulated SHG-FROG trace of a Gaussian pulse with pulse width 50 fs and spectrum centered at 800 nm.

Pulse retrieving from its SHG-FROG trace [54] is accomplished by implementing two-dimension phase-retrieval algorithm illustrated by the diagram shown in Fig. 3.3.2. Starting with a randomly guessed pulse profile $E(t)$, its SHG-FROG trace $S(\omega,\tau)$ can be computed. Compare this constructed FROG trace $S(\omega,\tau)$ with experimentally acquired FROG trace I_{FROG} by summing up the difference square of each matrix element, and the total is defined as the error G. If error is smaller than a pre-set threshold ε_0, then the current $E(t)$ can be considered as the final result of retrieving. Otherwise, the magnitude of the constructed FROG trace is replaced by the experimental data, leaving the phase of the constructed trace

untouched. Next, update the pulse profile $E(t)$ calculated from the modified FROG trace, and then proceed into the next iteration. Repeat this procedure until the error falls into the acceptable range.

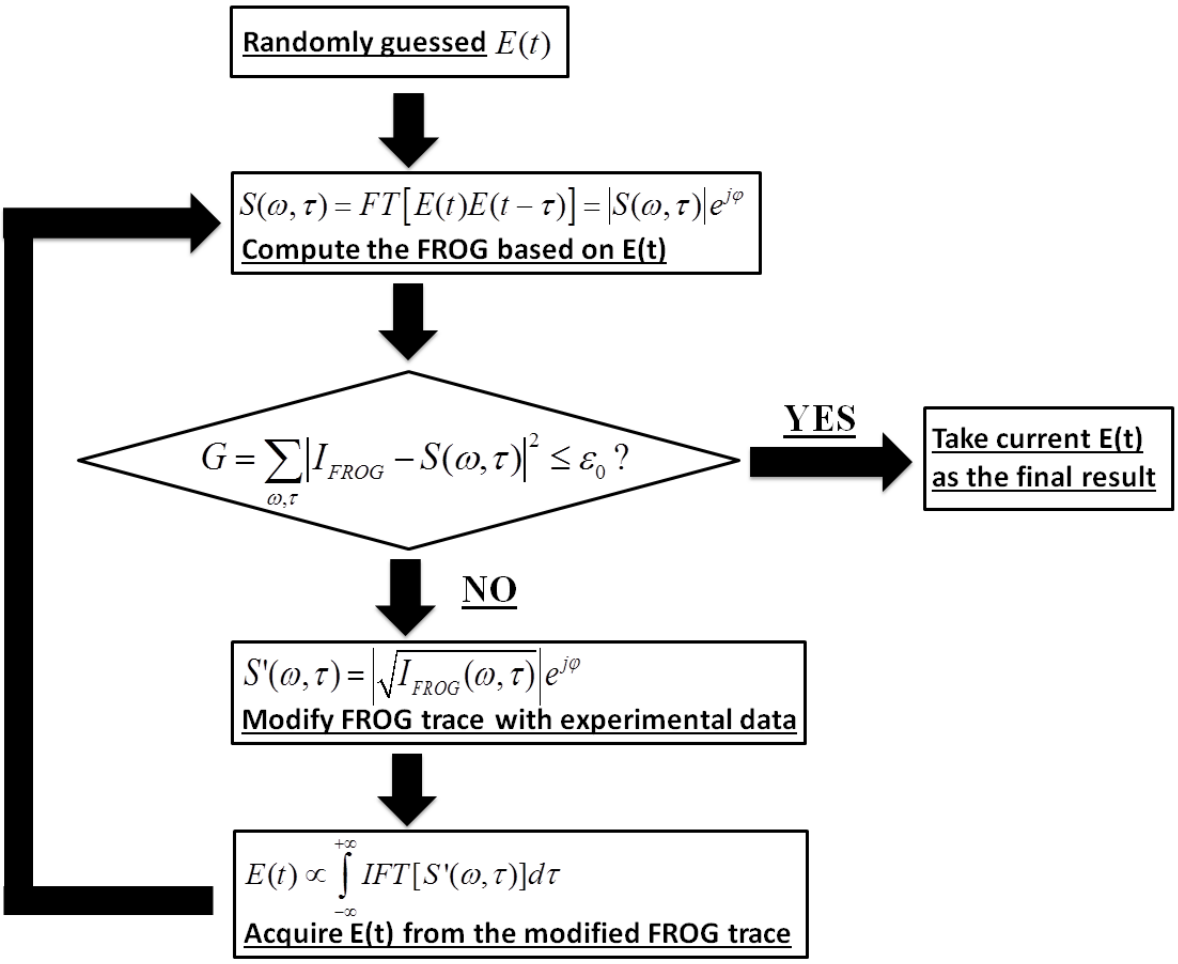

Figure 3.3.2 Flowchart showing the conventional FROG retrieving algorithm.

For some special applications, there is not enough space for the conventional FROG setup. For example, for nonlinear imaging microscopy or material processing

applications, the pulse properties at the focus of the objective lens have triggered a lot of interests. However, within such narrow space, shooting in two beams with tunable angle and placing a bulky nonlinear crystal is not an option. Therefore, collinear configuration of SHG-FROG was proposed [55]. Fig.3.3.3 illustrates the collinear FROG setup.

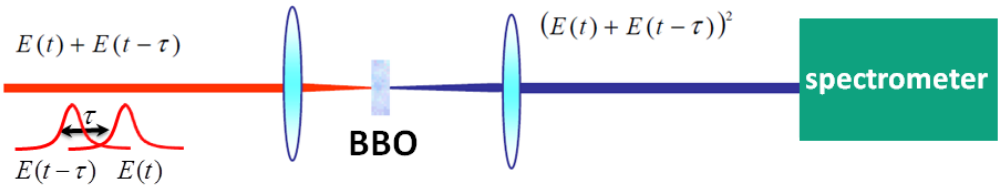

Figure 3.3.3 Schematic Diagram of a typical collinear SHG-FROG setup.

Compared with non-collinear conventional FROG, the SHG signal generated by each pulse itself is also included in the acquired FROG trace, resulting in interference fringes, which can be seen from the Eq. 3.3.2. [55]

$$I_{C-FROG}^{SHG}(\omega,\tau)=\left|\int_{-\infty}^{+\infty}[E(t)+E(t-\tau)]^2\exp(-i\omega t)dt\right|^2 \qquad (3.3.2)$$

The simulation result of a collinear SHG-FROG trace is shown in Fig. 3.3.4. When Fourier transform is applied to the collinear SHG-FROG trace along the delay τ dimension, three components can be separated according to their frequencies, as shown in Fig. 3.3.5. By applying a digital low-pass filter, the d.c. term, which is now at the center and well separated from any other high-frequency term, can be

taken out and, by applying inverse Fourier transform, the conventional non-collinear SHG-FROG can be acquired. Collinear FROG contains full information of non-collinear FROG.

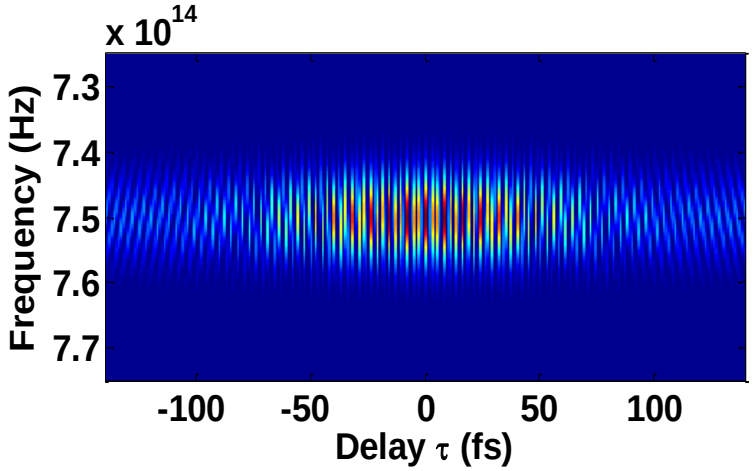

Figure 3.3.4 Simulated collinear SHG-FROG trace of a Gaussian pulse.

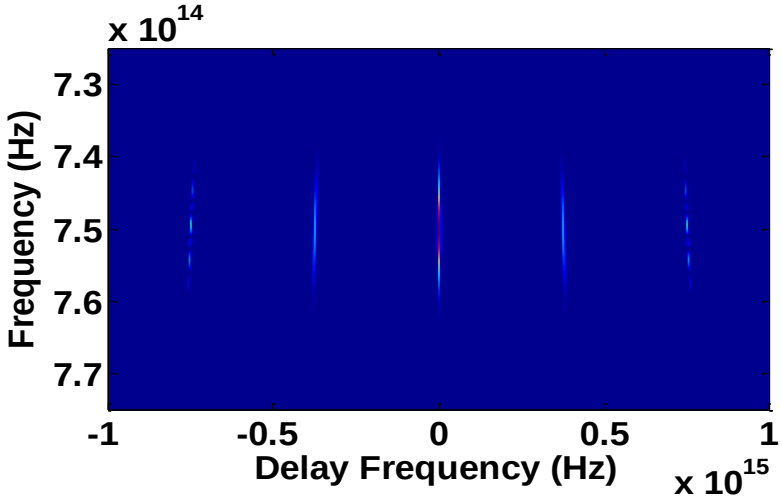

Figure 3.3.5 Fourier transform of the simulated collinear SHG-FROG in Fig. 3.3.4.

3.4 Holographic collinear FROG (HcFROG) for spatiotemporal characterizations of laser pulses

Critical information of light-matter interaction is prone to be contained in the amplitude and phase of optical near fields. Due to the remarkable progress of nanotechnology and ultrafast optics, optical fields are able to be investigated at unprecedented small and short spatiotemporal scales. More specifically, technique of scanning near-field optical microscopy has been used to explore optical fields in much more details than before. For example, by employing heterodyne interferometry, both the phase and amplitude of a standing evanescent wave was directly measured [56]. Authors of another report incorporated scanning near-field optical microscopy into one arm of a Mach-Zehnder interferometer to directly measure the intensity and phase of an evanescent wave at the base surface of a prism and a mode propagating inside a tapered fiber [57]. Furthermore, in order to mitigate the field perturbations and distortions introduced by the coupling between the sampled local mode and a propagating mode, second-order nonlinear optical effect is exploited. In 2010, our group proposed a solution of collinear frequency-resolved optical gating based on a second harmonic nanoprobe (SHARP) for *in-situ* characterizations of ultrafast laser pulses in the nano-femto spatiotemporal scale [58].

For pulse diagnostic approaches described above, one precondition is assumed that the spatial and temporal characteristics of the pulse being measured are independent. However, it is not always true that the error introduced by this

assumption is negligible. For example, when being focused by an objective lens with high numerical aperture, ultrafast pulses undergo modifications during their propagation, which may include temporal profile stretching due to group velocity dispersion (GVD), spectrum modification, and higher-order spectral phase distortion due to chromatic aberration. In these situations, the spatial and temporal characteristics of the pulse propagation are coupled with each other, and therefore the traditional approach of independent retrieving will no longer be accurate. To address this issue, we combine holography technique and collinear FROG method to jointly characterize the field at multiple locations to obtain the spatio-temporal evolution of the propagating pulse. Our system is built on a conventional collinear FROG setup [55] with a BBO crystal plugged into the fundamental beam path before the interferometer to generate a reference beam at second-harmonic wavelength. In the end this reference beam is recombined with the cFROG signal to generate holographic pattern, which is recorded by a spectrometer in the frequency domain. Phase at multiple locations are thus linked by the interference between the fixed reference beam and local cFROG trace. Therefore, by analyzing the holographic cFROG traces, the information of the pulse shape and phase at multiple locations can be retrieved jointly with a much simplified approach, and, what's the most important, since the phase are now linked with each other, actual phase differences between each two locations are retrievable, by which accurate and detailed information about the pulse propagation could be revealed.

Fig. 3.4.1 illustrates the model for the numerical simulation of this approach. Theoretically, as described by Eq. 3.4.1, a reference pulse term (marked by red square) has been added in the signal acquired by the spectrometer, resulting in the beating between the reference and the original collinear FROG trace (term marked by blue square). From the simulated result trace shown in Fig. 3.4.2 (a) we can see the interference fringes along both two dimensions. Fringes directed along wave frequency are due to the collinear configuration, and fringes along delay τ are due to the beating with the reference beam.

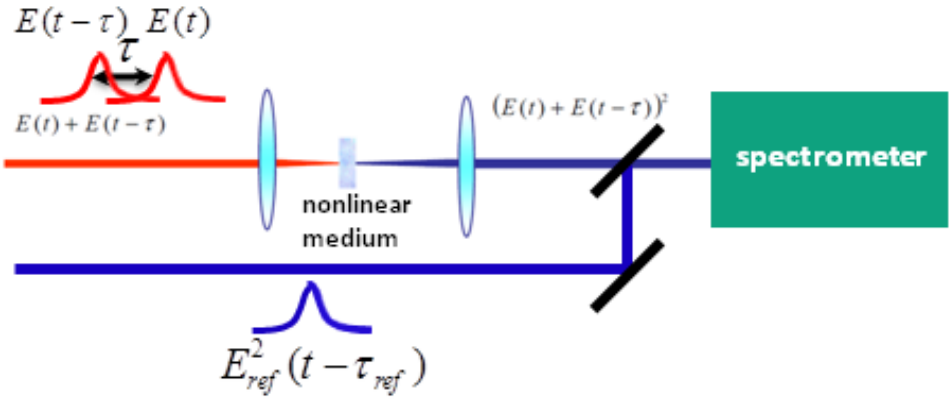

Figure 3.4.1 Model for the numerical simulation of the holographic collinear SHG-FROG experiment.

$$I_{HCFROG}(r,\Omega,\tau,\tau_R)=\left|E_{SHG}(r,\Omega)+E_{SHG}(r,\Omega)e^{i\Omega\tau}e^{i2\omega_0\tau}+E_{FROG}(r,\Omega,\tau)e^{i\omega_0\tau}+E^R_{SHG}(\Omega)e^{i\Omega\tau_R}e^{i2\omega_0\tau_R}\right|^2$$
$$=I_{FROG}(r,\Omega,\tau)+\left[E_{FROG}(r,\Omega,\tau)E^{R*}_{SHG}(\Omega)e^{i\omega_0\tau}e^{-i(\Omega+2\omega_0)\tau_R}+c.c.\right]+\ldots \quad (3.4.1)$$

By applying 2-D Fourier transform to the simulated trace in Fig.3.4.2 (a), different terms are isolated and represented by different spots in the two-dimension Fourier-transformed domain shown in Fig.3.4.2 (b).

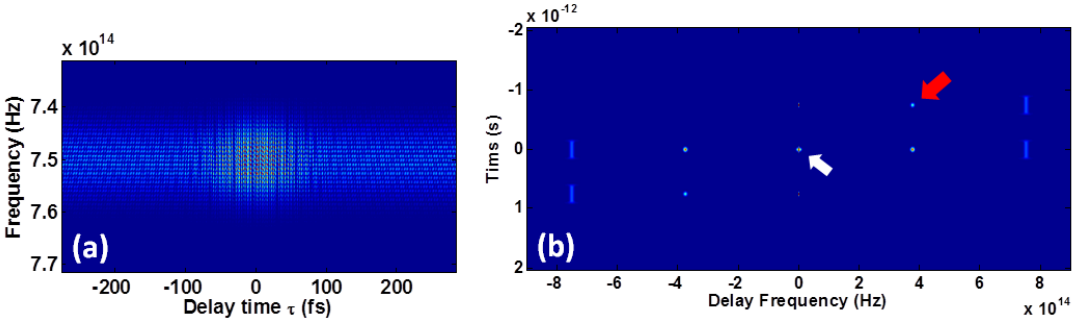

Figure 3.4.2 (a) Holographic collinear FROG (HcFROG) trace acquired by numerical simulation in the f-τ domain. (b) 2-D Fourier transform of the simulated HcFROG trace.

Compared with the Fourier-transformed collinear FROG trace in Fig.3.3.5, three extra spots (along with their symmetric components) exist due to the interference between the cFROG signal and the reference pulse. The spot pointed by white arrow is the DC component of the trace, from which the amplitude and the phase profile of the pulse can be retrieved. The spot pointed by red arrow is the beating between the FROG field and the second-harmonic reference field, and can be described as $b_i c^* = E_{FROG}(r_i, \Omega, \tau) E_{SHG}^{R*}(\Omega) e^{i[-\omega_0\tau + (2\omega_0+\Omega)\tau_R]}$, in which b_i is the FROG trace at location i and c^* is the conjugation of the second-harmonic reference field. Since the reference beam for the measurements at multiple locations has constant phase, the phase difference between location i and location j could be acquired by aligning and normalizing the beating term, as shown in Eq.3.4.2.

$$\Delta\varphi_{i,j} = \varphi_i - \varphi_j = \varphi\left(\frac{b_i}{b_j}\right) = \varphi\left(\frac{b_i c^*}{b_j c^*}\right) \quad (3.4.2)$$

Now with the pulse profile and phase retrieved at a location appointed as the pivot with the conventional FROG retrieving algorithm, the phase at all other locations can be directly recovered through Eq. 3.4.2. Since the conventional FROG retrieving is nothing more than recovering the phase distribution on the FROG trace, hereby we are able to retrieve the pulse information at all other locations without conducting any more time-consuming FROG retrieving. Most important, since now the phase at different locations are correlated by one reference beam, the spatial and temporal characteristics of the pulse are retrieved jointly. As a result, accurate and detailed information of the pulse propagation can be revealed.

As a proof-of-concept demonstration, we *in situ* characterize the pulse at the vicinity of the focus of an objective lens. The experimental setup diagram is shown in Fig.3.4.3. Femtosecond laser pulse (KMLabs, Central wavelength ~ 820nm, average output power ~400mW) is first focused onto a BBO crystal to generate a second-harmonic reference pulse. The reference pulse and the pump pulse are re-collimated and collinearly propagate until they are separated by a dichroic mirror (R400/T800). The reflected second-harmonic reference pulse is later delayed before being delivered into spectrometer. The transmitted fundamental pulse is delivered into a Michelson interferometer to generate two copies of the incoming pulse at the beamsplitter (Newport ultrafast beamsplitter UB.2), and the relative time delay τ between the two pulses can be tuned by shifting the mirror at the end of one arm,

which is mounted on a motorized translation stage. The two pulses are collinearly coupled into a Photonic Crystal Fiber (~10cm). The pulse output from the PCF is collimated by a 20× objective lens and then focused by another 40× objective lens. As shown by a dotted rectangle in Fig.3.4.3, these two objective lenses and the PCF output are positioned on the same motorized translation stage so they can translate jointly along axial direction, and therefore different axial locations around the focus of the lens could be measured with a fixed probe.

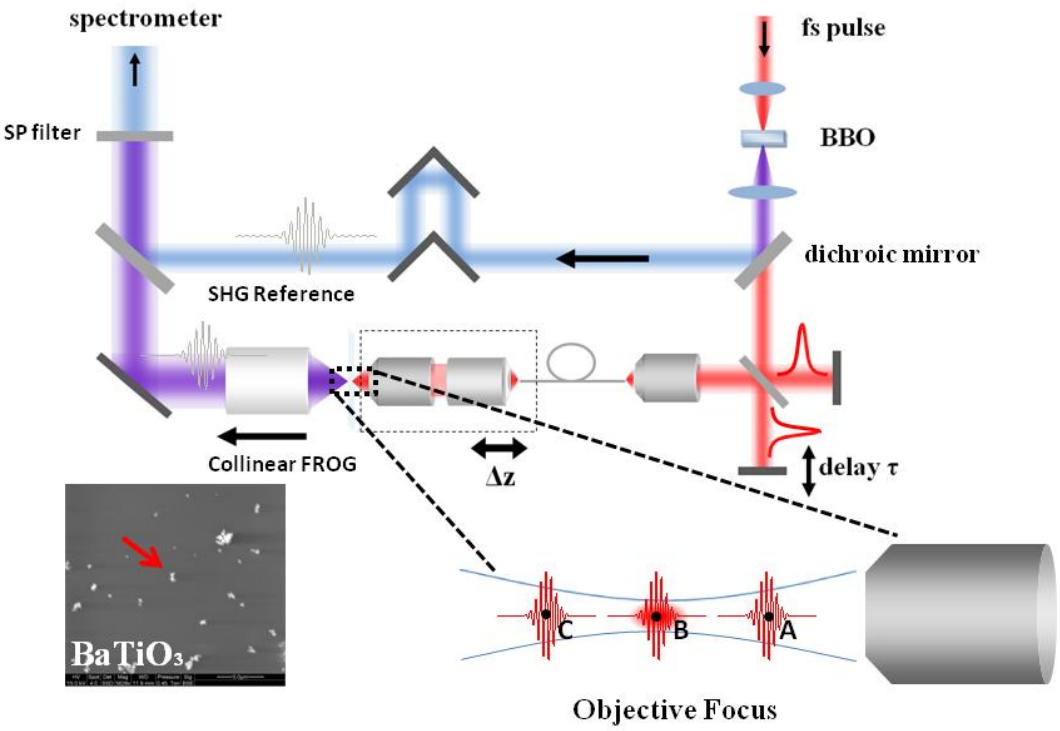

Figure 3.4.3 Schematic diagram of the holographic cFROG experiment setup. Left bottom inset: SEM image of the BaTiO3 nanocrystal cluster used as pulse characterization probe. Right bottom inset: distribution of a serious of locations to be measured.

The second-order nonlinear medium that the pulse is focused on is a $BaTiO_3$ micro cluster air-dried on a cover glass. Left bottom inset of Fig.3.4.3 shows its SEM image. The generated second-harmonic signal is then gathered and collimated by a long-working-distance objective lens (Mitutoyo 50× LWD), re-combined with the second-harmonic reference beam, filtered by a band-pass filter (D400/70, Chroma Technology), and finally be detected by a spectrograph with a liquid-nitrogen-cooled charge-coupled-device camera (SP2500i, Princeton Acton). The HcFROG trace is obtained by acquiring the spectrum of the incident signal as the delay time between the two pump pulses is scanned with an incremental step of 0.46 fs. Fig. 3.4.4 shows the photo of the actual experimental setup.

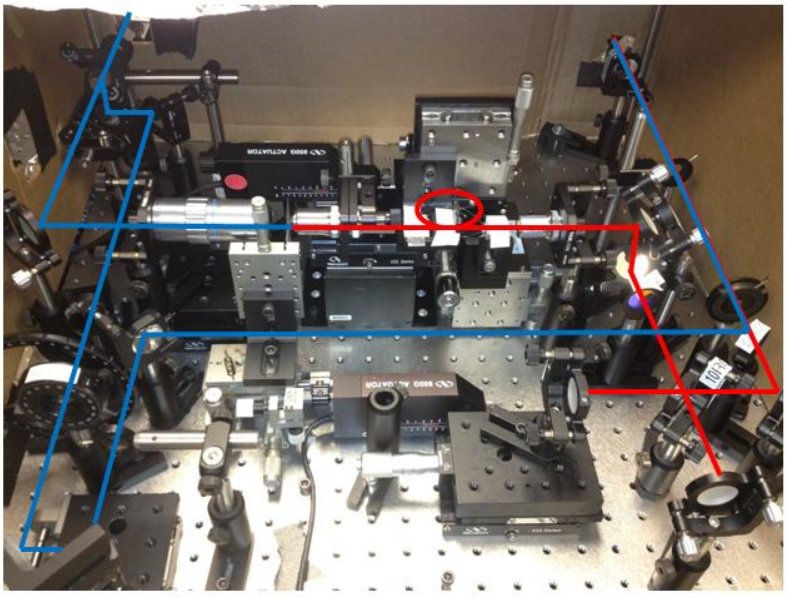

Figure 3.4.4 Photo of the holographic collinear FROG experimental setup.

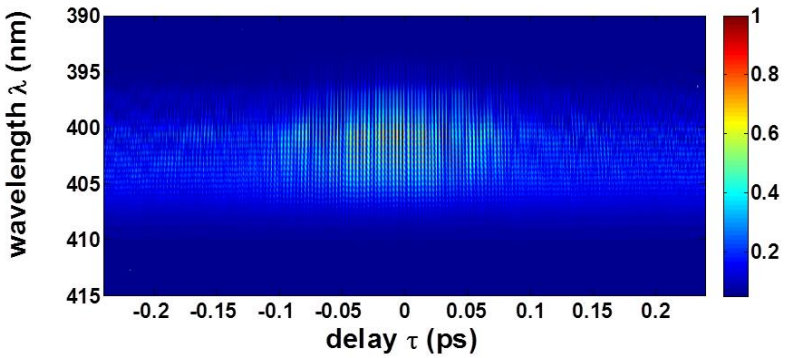

Figure 3.4.5 Holographic collinear FROG trace acquired by experiment in the λ-τ domain.

An obtained HcFROG trace is shown in the Fig.3.4.5. The HcFROG measurement is carried out at multiple locations on the optical axis through the focus of the objective lens while the delay of the reference beam is kept constant.

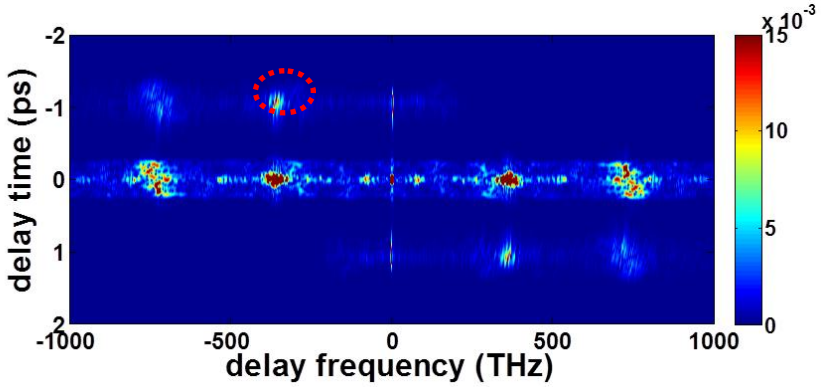

Figure 3.4.6 2-D Fourier transform of the HcFROG trace. The HcFROG trace acquired in the ω-τ domain has been transformed into the t-f domain (F.T. domain).

HcFROG traces in $\omega - \tau$ domain at three locations on the optical axis nearby the focus of the objective lens are acquired, and the data is processed as following:

1) Define a location as the pivot. Since the DC component of the experimentally acquired HcFROG trace is the (conventional) FROG trace of the pulse, by applying

super-Gaussian filter [59] to the HcFROG trace in its Fourier-transformed domain ($t-f$ domain), the FROG trace can be obtained. The pulse shape and the phase at the pivot are obtained by FROG retrieving algorithm described in section 3 of this chapter.

2) The (conventional) FROG traces at the rest two locations are obtained with the same filtering approach. By replacing the phase of these FROG traces with the phase of the pivot FROG trace modified by corresponding phase difference given by Eq. 3.4.2, the time-consuming phase retrieving can be eliminated and both the pulse shape and pulse phase are directly acquired from the updated FROG trace by directly implementing Eq. 3.4.3.

$$E(t)=\frac{\int E(t)E(t-\tau)d\tau}{\sqrt{\iint E(t)E(t-\tau)d\tau dt}} \qquad (3.4.3)$$

As shown in Fig.3.4.7, we have acquired pulse shapes and correlated phases at multiple locations through our holographic phase-retrieving approach. Both the retrieved and directly measured pulse spectrums are plotted in Fig.3.4.8 for comparison. Since the pulse phase at some location *i* could be Taylor-expanded as $\varphi_i(\Omega)=\varphi_i(\omega_0)+\varphi_i'(\omega_0)\Omega+\frac{1}{2}\varphi_i''(\omega_0)\Omega^2$, the phase difference between any two locations *i* and j could be written as Eq.3.4.4,

$$\Delta\varphi_{i,j}(\Omega) = \varphi_i(\Omega) - \varphi_j(\Omega) = [k_{i,j} + k_{i,j}{}'(\omega_0)\Omega + \frac{1}{2}k_{i,j}{}''(\omega_0)\Omega^2]\cdot\Delta z_{i,j}$$
$$= a_{i,j} + b_{i,j}\cdot\Omega + c_{i,j}\cdot\Omega^2 \qquad (3.4.4)$$

where $b_{i,j} = k_0{}'(\omega_0)\Delta z_{i,j}$ is the group delay obtained by fitting the phase difference $\Delta\varphi_{i,j}(\Omega)$ with a third-order polynomial (higher orders neglected).

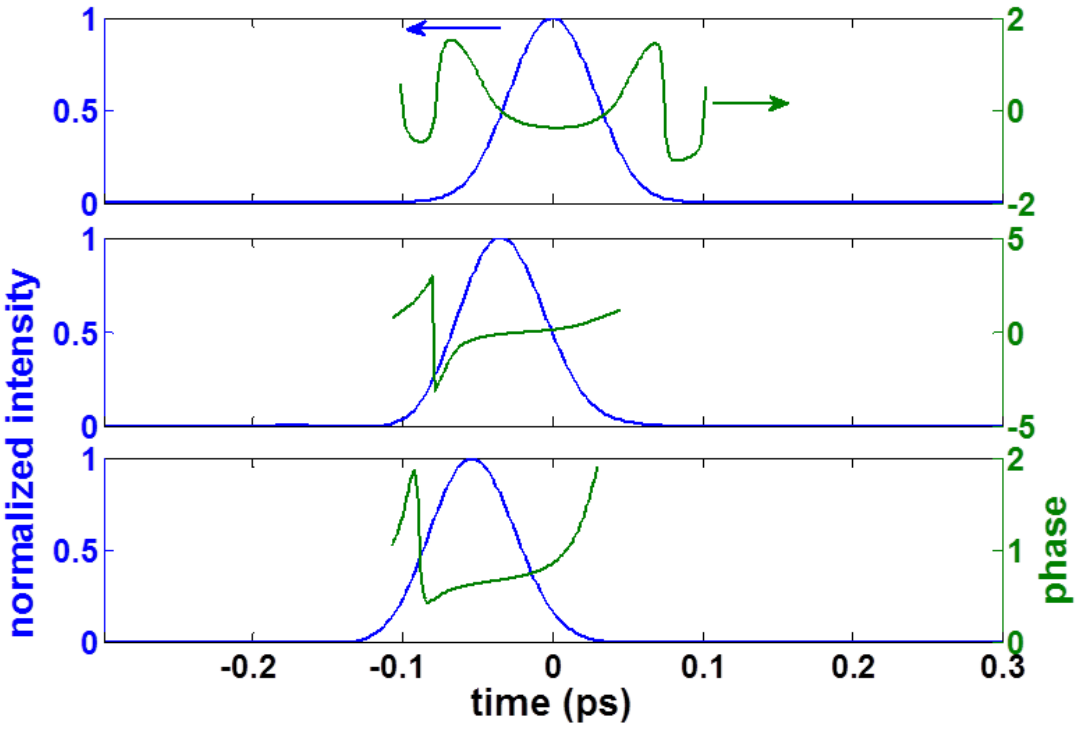

Figure 3.4.7 Jointly retrieved pulse shapes and phases at three different locations of measurement. The pulse propagation can be observed.

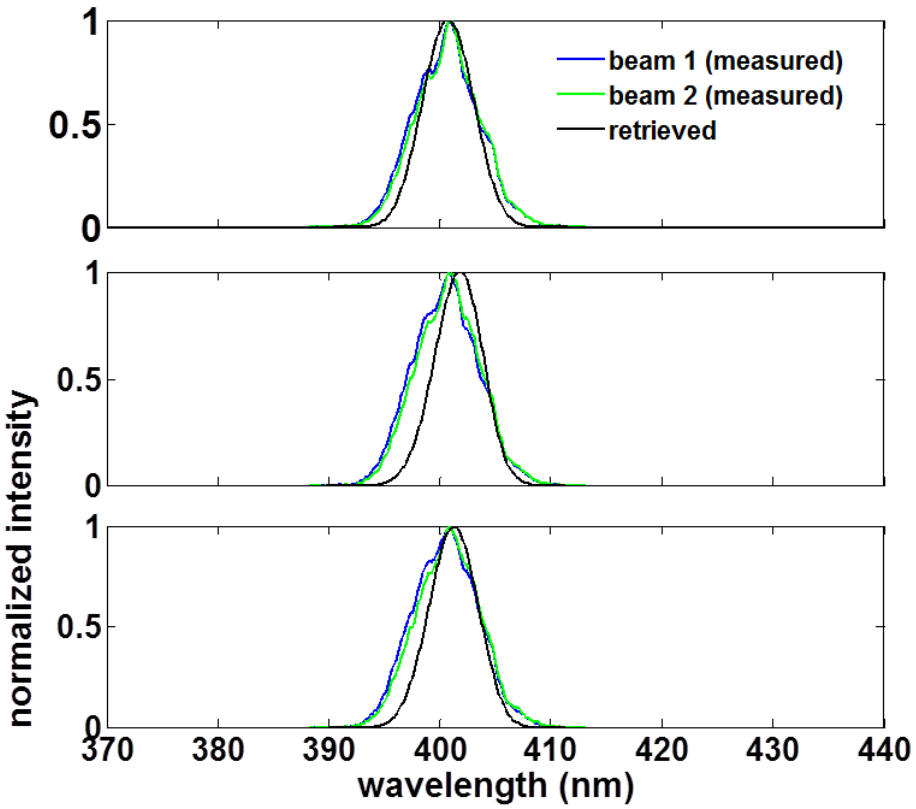

Figure 3.4.8 Comparison of the retrieved and measured spectrum of the second harmonic generated signal.

Fig.3.4.9 shows the phase differences between each two locations of measurement. Fig.3.4.10 shows the polynomial fitting to the phase differences and the resulted group delays. As a quick test on the validity of our group-delay measurement, we compare the experimentally recorded spatial pulse displacements (axial move of translation stage) with the retrieved group delay. As shown in Fig.3.4.11, the two sets of data match sufficiently well with each other.

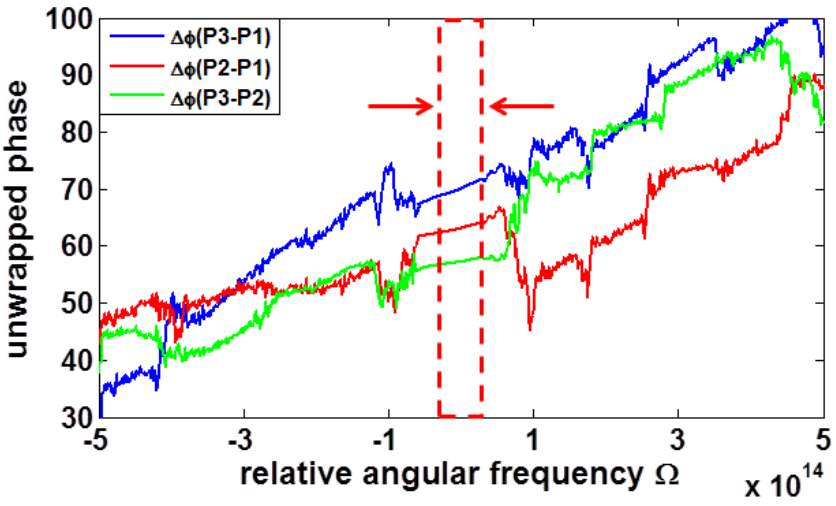

Figure 3.4.9 Unwrapped phase differences between each two measured locations as function of the wave angular frequency. The red dashed box marks the effective region of fitting.

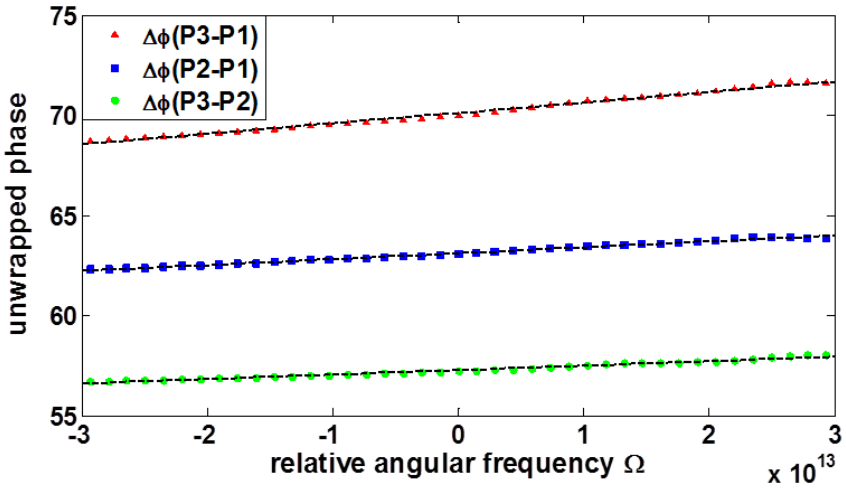

Figure 3.4.10 Third-order polynomial fitting of the phase difference from which the group delay and group velocity dispersion can be obtained.

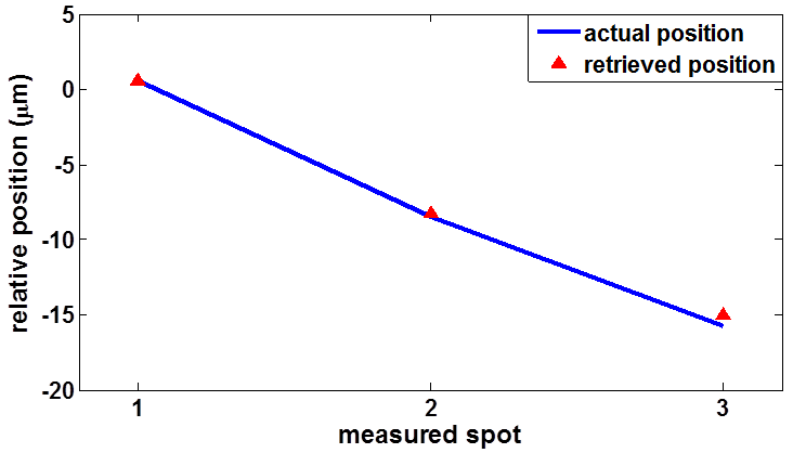

Figure 3.4.11 Comparison of the group delays retrieved from our approach and the directly recorded during experiment.

In conclusion, by applying holographic technique to the collinear FROG scheme, the retrieving of pulse shape and phase at a series of locations along the path of pulse propagation are not independent any more. They are now correlated through a reference beam, by which the spatial and temporal information of the pulse are retrieved jointly to accurately reveal more critical properties of the pulse propagation. As a demonstration, we characterized the field distribution in the vicinity of the focus of an objective lens. The retrieved results match well with the actual arrangements of the experiment. As a possible future development, our previous well-developed SHARP technique [58] can be combined with this holographic collinear FROG approach to significantly improve the efficiency and performance of the nano-femto scale spatiotemporal imaging of ultrafast optical near fields.

CHAPTER 4. G-FRESNEL DIFFRACTION OPTICAL DEVICE FOR SPECTROSCOPY APPLICATIONS

4.1 Introduction to miniature spectrometers

In the year of 1802, William Hyde Wollaston (1766 – 1828) used a lens to focus images of a narrow, sunlight-illuminated slit through a prism onto a screen. He observed the dark lines across the spectrum transverse to the dispersion direction [60]. Meanwhile, William Herschel (1738 – 1822) discovered the infra-red radiation by the rise in temperature of the bulb of a thermometer [61]. Joseph von Fraunhofer (1787 – 1826) invented spectroscope in 1814 and he discovered 574 dark fixed lines in the solar spectrum [62]. In 1859, Gustav Kirchhoff and Robert Bunsen in the University of Heidelberg made reasonable explanation that the vapor in the atmosphere of the sun absorbs lines on spectrum of the continuous white light [63]. These lines are still called ‘Fraunhofer lines’ today in his honor. Since these years, the fundamental structure of spectroscope – the sequence of collimator, dispersion component and focusing component – has changed little.

In modern years, optical spectrometer is one of the most widely used scientific instruments in a variety of research fields. Through my entire Ph.D. research work, spectroscopy has been a critical method for optical signal analyses. Usually a modern optical spectrometer needs to realize three functions in series: **collimation**, **dispersion** and **focusing**, among which collimation and focusing are

usually done by lens or curved mirrors, and dispersion is done by diffractive gratings. Most traditional-style optical spectrometers are composed of several discrete optical elements making the instruments expensive and often bulky. Meanwhile, there exists a growing demand to miniaturize spectrometers to create portable as well as affordable devices for use in remote in-the-field locations for applications, such as, in biomedical sample and disease diagnosis. One existing approach used to address these demands is to combine the functions of several optical elements to reduce the complexity of the interior layout of a spectrometer, for example by use of a curved grating [64] or volume holograms [65]. Another approach is to employ micro-fabrication technology, to develop devices such as a waveguide grating coupler and integrated spectrometers based upon microelectromechanical (MEMS) systems [66].

4.2Hybrid diffractive optical element G-Fresnel

We demonstrate the use of a hybrid grating-Fresnel diffractive optical element we named G-Fresnel, which realizes in a single device collimation, dispersion and collection through combining the featured patterns of a grating and a Fresnel lens into a single thin-film element. In particular, a G-Fresnel device prototype was demonstrated by using polydimethylsiloxane (PDMS) soft lithography [67 - 70] which fuses the functions of a grating and a Fresnel lens into one hybrid device. Compared with existing devices, the G-Fresnel has two major advantages. First, it can have a smaller f/# (or large numerical aperture) compared with a

conventional concave grating, and can therefore potentially result in a more compact spectrometer without significantly sacrificing the resolution. Second, the device has planar surface structures and hence can potentially allow for low-cost mass production by replicating from a master pattern.

As for the design principle of G-Fresnel, in order to possess the dual properties of a lens and a grating, the desired field transmission (or reflection) coefficient of a diffractive optical element may be given by

$$t(x,y) \propto \eta(\lambda) e^{-j\frac{\pi}{\lambda F}(x^2+y^2)} e^{j\frac{2\pi}{\Lambda}x} \qquad (4.2.1)$$

where λ is the wavelength, F is the focal length at λ, Λ is the grating period, and η represents the diffraction efficiency of the device. Since Eq.4.2.1 comprises the product of the transmittances of a Fresnel lens and a linear grating, the diffractive optical element is referred to as G-Fresnel in the following. Let us consider a point source located at (x_0, y_0, -d) (c.f., Fig.4.2.1). Under the paraxial approximation, the field distribution after the G-Fresnel can be obtained by applying the Fresnel diffraction formula [71] and is given by

$$\begin{aligned} f(x,y,z) &\propto \iint e^{j\frac{\pi}{\lambda d}\left[(x'-x_0)^2+(y'-y_0)^2\right]} p(x',y') e^{-j\frac{\pi}{\lambda F}\left(x'^2+y'^2\right)} e^{j\frac{2\pi}{\Lambda}x'} e^{j\frac{\pi}{\lambda z}\left[(x-x')^2+(y-y')^2\right]} dx'dy' \\ &\propto \iint e^{j\frac{\pi}{\lambda}\left(\frac{1}{d}-\frac{1}{F}+\frac{1}{z}\right)\left(x'^2+y'^2\right)} p(x',y') e^{-j2\pi\left[\left(\frac{x_0}{\lambda d}-\frac{1}{\Lambda}+\frac{x}{\lambda z}\right)x'+\left(\frac{y_0}{\lambda d}+\frac{y}{\lambda z}\right)y'\right]} dx'dy' \end{aligned} \qquad (4.2.2)$$

where p(x, y) is the pupil function of the G-Fresnel. It can be shown that the geometrical image of the point source is located at (x_i, y_i, L), where

$$x_i = -\frac{L}{d}x_0 + L\frac{\lambda}{\Lambda}, y_i = -\frac{L}{d}y_0, L = \frac{Fd}{d-F} = \frac{d}{\lambda d/\lambda_0 F_0 - 1} \quad (4.2.3)$$

and λ_0 and F_0 are the design wavelength and design focus length of the G-Fresnel respectively (note: $\lambda F = \lambda_0 F_0$). Therefore, a G-Fresnel can both image a point source (i.e., lens property) and disperse its different wavelength components (i.e., grating property). It can be shown from Eq.4.2.3 that a linear relationship holds between x_i and L, i.e.,

$$L = \frac{\Lambda d}{\lambda_0 F_0 - x_0 \Lambda} x_i - \frac{\lambda_0 F_0 d}{\lambda_0 F_0 - x_0 \Lambda} \quad (4.2.4)$$

In other words, the foci of the different wavelengths lie on a line with a slope dL/dx_i given by $\frac{\Lambda d}{\lambda_0 F_0 - x_0 \Lambda}$.

Note that Eq.4.2.1 can be rewritten as

$$t(x,y) \propto \eta(\lambda) e^{j\frac{\pi}{\lambda F}x_c^2} e^{-j\frac{\pi}{\lambda F}\left[(x-x_c)^2+y^2\right]} \quad (4.2.5)$$

where $x_c = \lambda F/\Lambda$. In other words, a G-Fresnel is equivalent to an off-axis Fresnel lens with its center shifted to $(x_c, 0)$. However, since the circular grating of a Fresnel lens is chirped and its period is inversely proportional to the distance from the center,

such off-axis Fresnel lens becomes increasingly challenging to fabricate for large x_c. For instance, consider a grating period $\Lambda \sim \lambda$. The effective center shift is given by $x_c \sim F$, which would require a large Fresnel lens with sub-wavelength features.

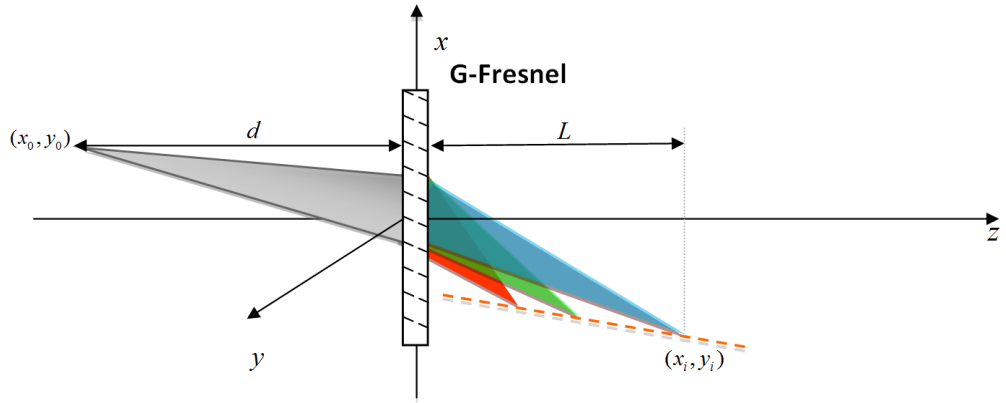

Figure 4.2.1 Schematic diagram illustrating the dual focusing and dispersing properties of a transmission-type G-Fresnel.

The G-Fresnel can also be interpreted as a thin hologram. As shown in Fig.4.2.2, let us consider a thin hologram recorded by a diverging spherical reference wave $e^{j\frac{\pi}{\lambda l}(x^2+y^2)}$ and a converging signal wave $e^{-j\frac{\pi}{\lambda l}[(x-\Delta x)^2+y^2]}$, where l is the distance between each point source and the recording medium and Δx is the relative displacement (along the x axis) between the two point sources. The transmittance t_H of the hologram is given by

$$
\begin{aligned}
t_H &\propto \left| e^{j\frac{\pi}{\lambda l}\left(x^2+y^2\right)} + e^{-j\frac{\pi}{\lambda l}\left[(x-\Delta x)^2+y^2\right]} \right|^2 \\
&= 2 + \left\{ e^{-j\frac{\pi}{\lambda l}\left(x^2+y^2\right)} e^{-j\frac{\pi}{\lambda l}\left[(x-\Delta x)^2+y^2\right]} + c.c. \right\} \\
&= 2 + \left[e^{-j\frac{\pi}{\lambda l}\Delta x^2} e^{-j\frac{2\pi}{\lambda l}\left(x^2+y^2\right)} e^{j\frac{2\pi}{\lambda l/\Delta x}x} + c.c. \right]
\end{aligned}
\qquad (4.2.6)
$$

The first term in the bracket of Eq.4.2.6 (second line) is essentially a G-Fresnel if we identify $F = l/2$ and $\Lambda = \lambda l / \Delta x$.

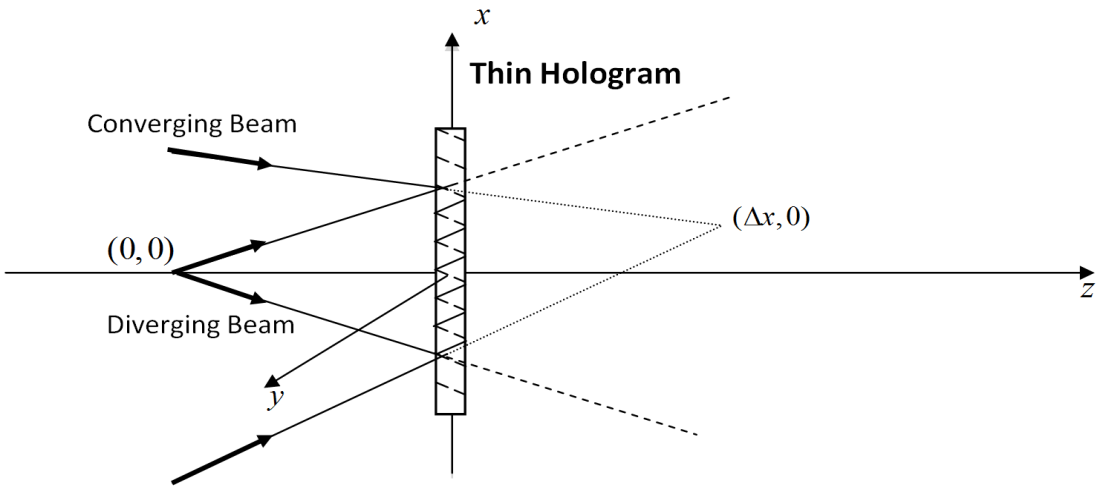

Figure 4.2.2 Schematic diagram showing a thin hologram recorded with diverging and converging spherical waves.

The G-Fresnel can be fabricated holographically as illustrated by Fig.4.2.2. However, a thin hologram also contains a conjugate term (c.f.Eq.4.2.6) and usually has limited diffraction efficiency. Here we describe a simple method to fabricate the G-Fresnel by using PDMS soft-lithography [72]. The fabrication procedure is illustrated in Fig.4.2.3. Briefly, PDMS pre-polymer mix (Dow Corning, Sylgard-184

PDMS, base to curing agent weight ratio 10:1) is poured onto the surface of a Fresnel lens (c.f. Fig.4.2.3 (a)). After it is *in situ* cured at room temperature for two days, a negative Fresnel lens mold is formed and can be peeled off (c.f. Fig.4.2.3 (b)). Fig.4.2.3 (f) shows a negative Fresnel mold fabricated this way. We then sandwich the PDMS pre-polymer between the negative Fresnel mold and a grating (Newport, 300lines/mm) (c.f. Fig.4.2.3(c)). The grating is mounted on a linear translational stage, which can be used to adjust the distance between the two molds and hence the device thickness. After curing it for about two days at room temperature, a transmission-type G-Fresnel is fabricated (c.f. Fig.4.2.3 (d)). A photo of a transmission-type G-Fresnel fabricated by using such method is shown in Fig.4.2.3 (g). A reflection-type G-Fresnel can be readily obtained by coating the grating side of a transmission-type G-Fresnel with a thin layer of reflective film as illustrated in Fig.4.2.3 (e). Fig.4.2.3 (h) shows a photo of reflection-type G-Fresnel, of which the grating side was coated with a layer of 50-nm-thick Au film by using a sputtering system (Kurt Lesker CMS-18/RF).

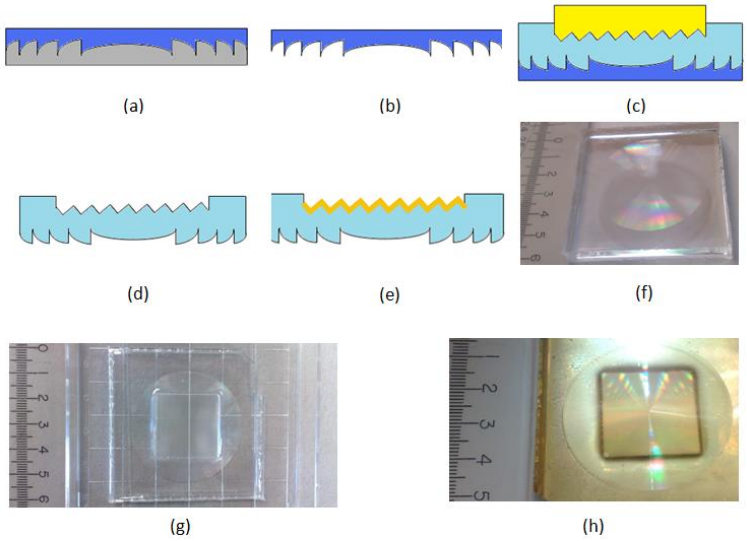

Figure 4.2.3 Schematic diagram illustrating the procedure of fabricating a G-Fresnel; (a): PDMS pre-polymer mix is poured onto the surface of a Fresnel lens; (b): after it is in situ cured, a negative Fresnel lens mold is formed and can be peeled off; (c) PDMS pre-polymer is sandwiched between the negative Fresnel mold and a grating; (d): after curing a transmission-type G-Fresnel is fabricated; (e): a reflection-type G-Fresnel can be readily obtained by coating the grating side of a transmission-type G-Fresnel with a thin layer of reflective film; (f): a photo of a fabricated negative Fresnel mold; (g): a photo of a fabricated transmission-type G-Fresnel (h): a photo of a fabricated reflection-type G-Fresnel (Fresnel surface on top).

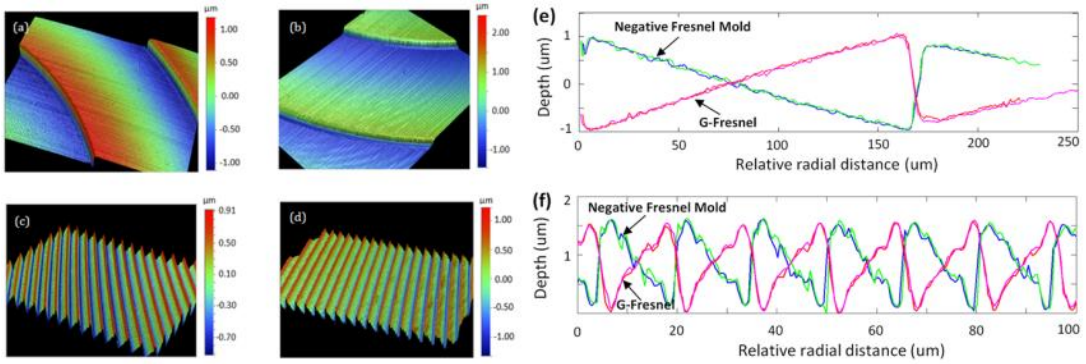

Figure 4.2.4 Typical surface profiles of a negative Fresnel mold and the Fresnel side of a G-Fresnel measured by optical profilometry. (a) and (b): 3D surface profile near the central parts of a negative Fresnel mold and the Fresnel side of a G-Fresnel respectively; (c) and (d): 3D surface profiles near the peripheral parts of the negative mold and the G-Fresnel respectively; (e) comparison of surface height profiles along the radial direction near the central parts of the mold and the G-Fresnel; (f) comparison of surface height profiles along the radial direction near the peripheral parts of the mold and the G-Fresnel.

In order to examine the quality of the fabricated G-Fresnel devices, we utilized a profilometer (WYKO NT1100) to measure the three-dimensional (3D) surface profiles of a negative Fresnel mold as well as the Fresnel side of a fabricated G-Fresnel. The results are given in Fig.4.2.4, in which (a) and (b) show the typical 3D surface profiles near the central parts of the negative mold and the Fresnel side (of the G-Fresnel) respectively while (c) and (d) show those near the periphery. Fig.4.2.4 (e, f) further show the typical surface height profiles along the radial direction near the central and peripheral parts of both devices. For the purpose of comparison, these plots are shifted by arbitrary amounts in order to align with each other. As expected, the height profiles of the negative Fresnel mold and the G-Fresnel (Fresnel side) exhibit anti-correlation. Clearly, good-fidelity pattern transfer from the mold to the G-Fresnel is achieved.

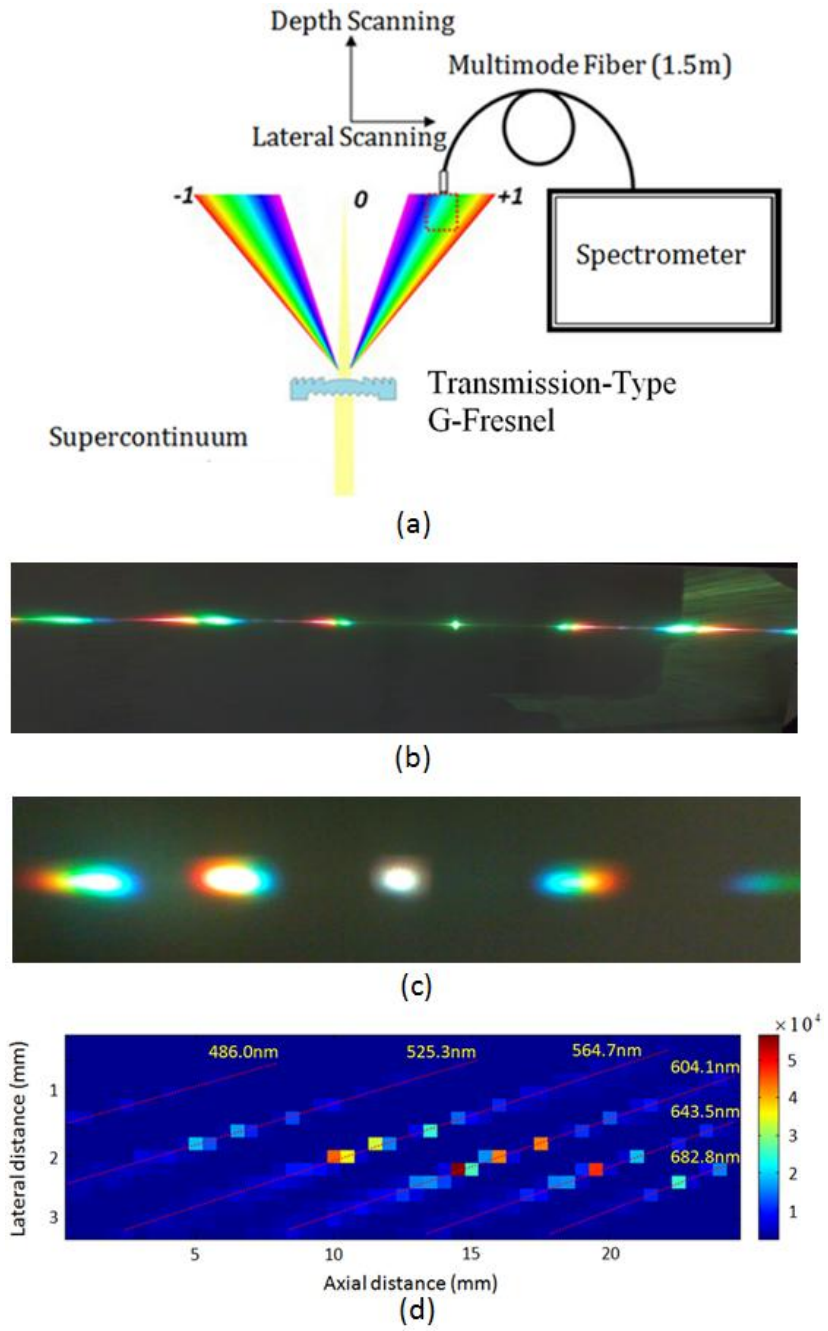

Figure 4.2.5 Optical characterization results; (a) schematic diagram of the experimental system; (b) a photo of a focused diffraction pattern produced by passing a collimated supercontinuum through a transmission-type G-Fresnel; (c) diffraction pattern produced by a grating; (d) measured intensity distribution of several exemplary wavelengths (486.0 nm, 525.3 nm, 564.7 nm, 604.1 nm, 643.5 nm, 682.8 nm).

We have also performed optical characterization of a transmission-type G-Fresnel (shown in Fig.4.2.5) by utilizing white light supercontinuum [73] generated by femtosecond laser pulses in a highly nonlinear photonic crystal fiber [74]. Fig. 4.2.5(a) illustrates the schematic diagram of the experimental system. Briefly, a collimated supercontinuum beam (diameter: ~10 mm) was incident on the transmission-type G-Fresnel. The transmitted beam became focused and consisted of several diffraction orders as shown in Fig.4.2.5 (b). The central focused bright spot corresponds to the zero's order, i.e., directly transmitted beam, while the rainbows on both sides correspond to higher diffraction orders (± 1, ± 2…, etc). On the contrary, if the collimated supercontinuum is directly incident on a planar grating, only unfocused diffraction pattern can be produced as shown in Fig. 4.2.5 (c). To further study this dual focusing and dispersion properties, we utilized a multimode optical fiber as a probe, which was placed behind the transmission-type G-Fresnel and scanned in two dimensions (i.e., along the axial and one lateral directions as illustrated in Fig.4.2.5 (a)) by using motorized translational stages. The scanning covered an area of 4 mm (lateral) x 25 mm (axial). The output of the multimode fiber was detected by a spectrometer (PI/Acton SpectraPro 2500 with a liquid nitrogen cooled charge coupled device detector PI/Acton Spec-10). Fig. 4.2.5 (d) presents the measured intensity distribution of several wavelength components. It shows that different wavelengths were focused by the transmission-type G-Fresnel and that they propagated along different directions. Our results clearly demonstrate that the G-

Fresnel has the dual properties of a grating and a Fresnel lens, and can therefore both disperse and focus light. Note that according to Eq.4.2.4, the foci trace of the different wavelengths is parallel with the optical axis (z), as a collimated supercontinuum was used. This is in agreement with the measured result shown in Fig. 4.2.5(d).

As a summary of this section, the G-Fresnel device is demonstrated. G-Fresnel has the dual functionalities of a grating and a Fresnel lens. We showed in theoretical analysis that the G-Fresnel can both image a point source and disperse its various wavelength components. Double-sided transmission and reflection type G-Fresnel devices were fabricated by using PDMS based soft lithography. We also performed 3D surface profilometric measurements to evaluate the quality of the fabricated devices. Finally, optical characterization was performed to experimentally verify the dual focusing and dispersing properties of this device. With its potential for mass production through surface pattern replication and the possibility of achieving small f/#, the G-Fresnel can open a promising avenue for developing cost-effective, compact, and portable optical spectrometers. In addition, considering that it can be easily integrated with the optofluidic devices fabricated by PDMS soft lithography, we believe that the G-Fresnel can also find exciting applications in the emerging field of optofluidics [75] such as on-chip spectroscopy.

4.3 Demonstration of the miniature spectrometer prototype based on G-Fresnel

As mentioned in prior sections, the advantages of the G-Fresnel are three-fold: first, it combines the functions of **collimation, dispersion** and **collection** in a single thin-film element; second, it can have a low f-number, leading to a compact system; third, it may be realized by surface relief patterning, opening the possibility of low-cost volume production through replicating from a master pattern. Here we explore the G-Fresnel based optical spectrometer both theoretically and experimentally. Our simulation shows that a spectral resolution of about 1 nm can be achieved by using a compact G-Fresnel (diameter ~ 4 mm, focal length, 1 cm). A proof-of-concept spectrometer implemented with a G-Fresnel is also experimentally demonstrated.

Let us consider a transmission-type G-Fresnel diffractive optical element. To achieve a dual functionality of dispersion and focusing, its transmittance is specified by $T(x,y) = T_G(x,y)T_F(x,y)$, where $T_G(x,y)$ represents the transmittance of a constituent grating and $T_F(x,y)$ denotes that of a constituent Fresnel lens. Both the grating and the Fresnel lens can be realized by surface relief pattern and their transmittances are given by

$$T_i(x,y) = e^{j\frac{2\pi}{\lambda}(n-1)h_i(x,y)} \quad (i = G \quad or \quad F) \qquad (4.3.1)$$

in which λ is the wavelength, n is the refractive index of the substrate material, and h_G and h_F are the respective surface height profiles. The G-Fresnel can be implemented by either placing the grating and the Fresnel lens separately on opposite sides (double-sided), or alternatively, superimposing them in one side of the device (single-sided). Fig.4.3.1 shows the central portion of computer-generated surface profiles of a double-sided G-Fresnel (Fig. 4.3.1(a)), and alternatively a single-sided one whose surface height is a synthesis of those of the constituent grating and Fresnel lens, i.e. $h(x,y) = h_G(x,y) + h_F(x,y)$ (Fig. 4.3.1(b)).

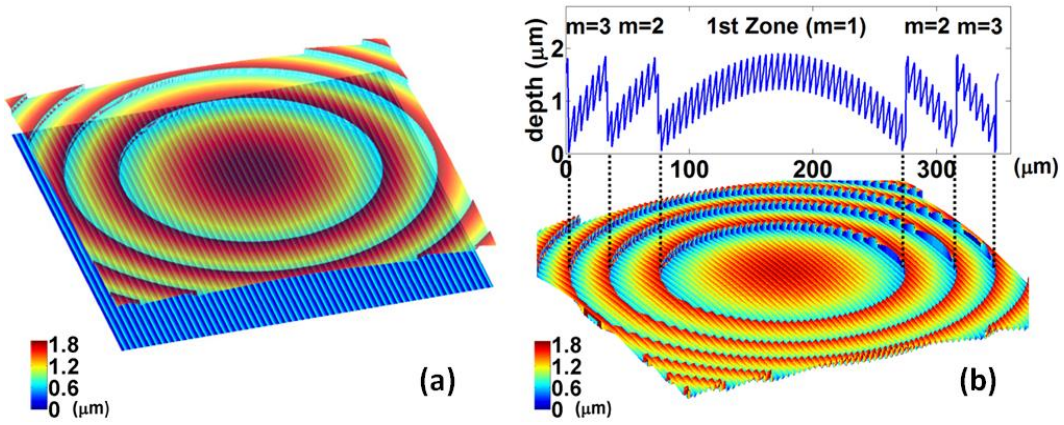

Figure 4.3.1 Computer-generated surface profile (central part) of a double-sided miniature G-Fresnel (a) and a single-sided miniature G-Fresnel (b).

In our simulation, the grating profile $h_G(x,y)$ is selected to be a periodic saw wave with a pitch of 200 grooves per mm. The constituent continuous-relief Fresnel lens has a focal length of f_0 = 1 cm at the design wavelength of λ_0 = 500 nm, and a diameter of 4.096 mm (corresponding to f-number ~ 2.4). A key advantage of the G-

Fresnel is that a small f-number can be realized in a thin-film element, opening the possibility of an ultra-compact spectrometer. The surface height profile of the constituent Fresnel lens is given by [76]

$$h_F(x,y) = \frac{m\lambda_0 - (\sqrt{x^2 + y^2 + f_0^2} - f_0)}{n-1}$$
$$((m-1)\lambda_0 \le \sqrt{x^2 + y^2 + f_0^2} - f_0 < m\lambda_0) \qquad (4.3.2)$$

where $m = 1, 2, 3...M$ is the Fresnel zone number.

To quantitatively evaluate the achievable spectral resolution, a monochromatic point source is hypothetically placed at 2 cm (i.e., $2f_0$) away from the G-Fresnel (Fig.4.3.2 (a)). The field $U_0(x,y)$ immediately after the G-Fresnel $(z = 0)$ is given by

$$U_0(x,y) \propto \frac{\exp(jkr)}{r} P(x,y)T(x,y) \qquad (4.3.3)$$

$$r = \sqrt{(2f_0)^2 + x^2 + y^2} \qquad (4.3.4)$$

where $P(x,y)$ is the pupil function. The field $U_1(x,y,z)$ behind the G-Fresnel can then be obtained by applying the Huygens-Fresnel Principle [68].

$$U_1(x,y,z) \propto \frac{1}{j\lambda} \iint_{\Sigma} U_0(\xi,\eta) \frac{\exp(jkr_{01})}{r_{01}} \cos\theta d\xi d\eta \qquad (4.3.5)$$

$$r = \sqrt{(x-\xi)^2 + (y-\eta)^2 + z^2} \qquad (4.3.6)$$

$$\cos\theta = z / r_{01} \tag{4.3.7}$$

We first calculated the intensity distribution in a region surrounding the geometric image [1.9 mm ≤ x ≤ 2.1 mm and 18.7 mm ≤ z ≤ 21.3 mm, see the rectangle marked in Fig.4.3.2 (a)]. The 1st-order diffraction patterns (summed up in y direction) at three representative wavelengths (490 nm, 500 nm and 510 nm) are shown in Fig.4.3.2 (b). The dual functionality of focusing and dispersion of the designed G-Fresnel can be clearly observed. The foci of different wavelengths are found to be located along a tilted line with a slope given by $dx / dz = \lambda_0 f_0 / (\Lambda d) = 0.5$, where $d = 2 f_0$ and Λ is the grating period [19]. Let us assume that an arrayed detector (pixel pitch: 5 μm) is placed along the line (Fig. 4.3.2 (b)). By optimizing the intercept while maintaining the slope, the point spread functions on the hypothetical detector at multiple wavelengths (from 496 nm to 504 nm with 1 nm separation) can be calculated and are plotted in Fig.4.3.2(c), which indicates that a spectral resolution of approximately 1 nm can be achieved. It should be noted that similar analysis could also be applied to a reflection-type G-Fresnel, which can fold the optical beam path and result in a more compact design.

We have also conducted proof-of-concept experimental study to demonstrate the feasibility of a G-Fresnel based spectrometer. We utilized PDMS soft lithography [77] to fabricate a prototype double-sided transmission-type G-Fresnel. The detailed fabrication procedure and characterization results were described in the

previous section and Ref. 19. A double-sided transmission-type G-Fresnel was fabricated as shown in Fig.4.3.3 (b) with a device area of about 1 in. × 1 in. (2.54 cm × 2.54 cm).

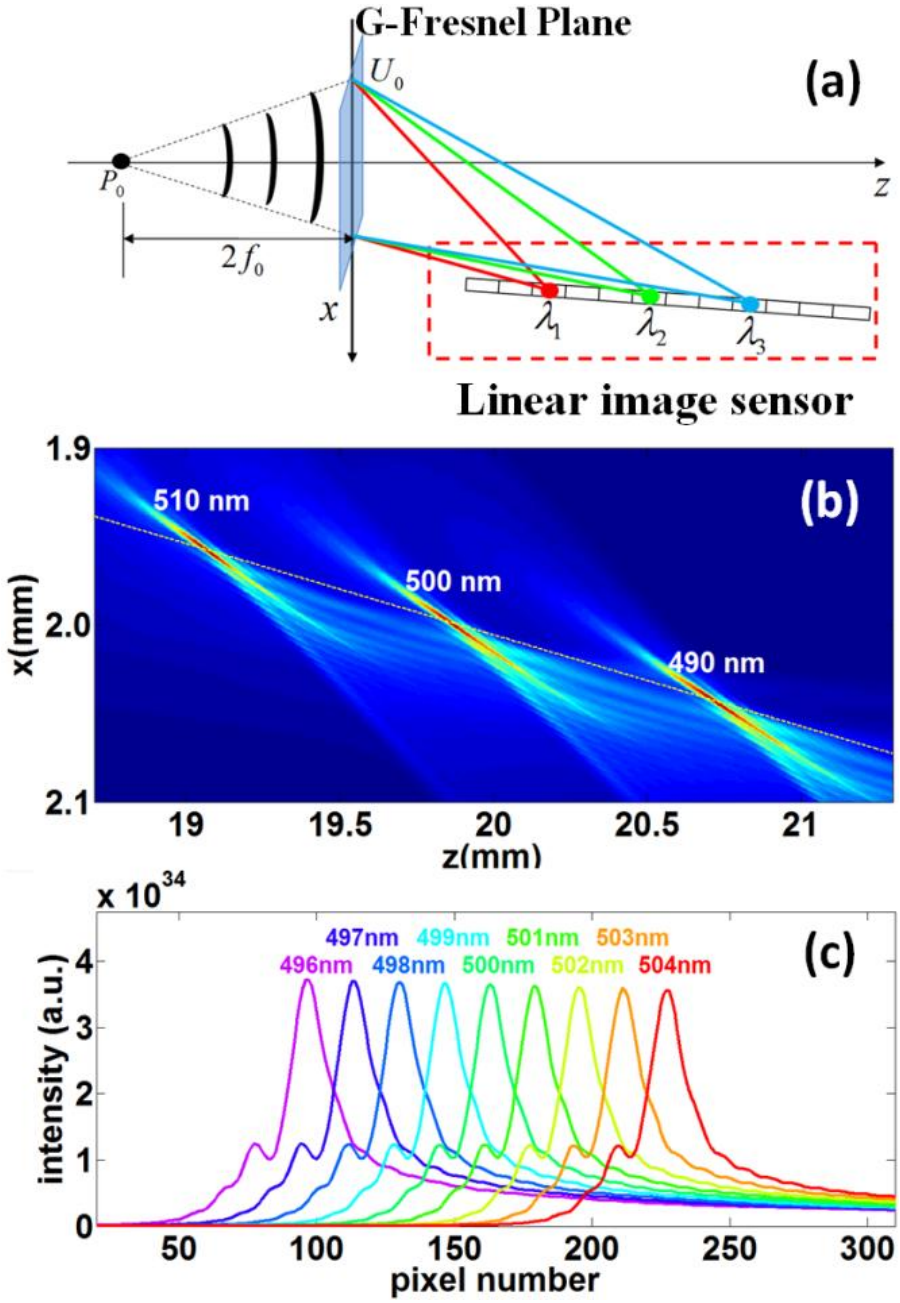

Figure 4.3.2 (a) Schematic diagram illustrating the geometric configuration used in our simulation; (b) intensity distribution of the 1st order diffraction patterns at three representative wavelengths (490 nm, 500 nm, 510 nm); locus of the foci can be fitted with a dotted line; (c) Calculated point spread functions at multiple wavelengths (496 nm -504 nm) on a tilted hypothetical detector with its position optimized to match with the experimental result shown in Fig.4.3.3(c).

A proof-of-concept spectrometer was then built on an optical table as illustrated in Fig.4.3.3 (a). It consists of an entrance slit, the G-Fresnel (Fig.4.3.3 (b)), and a CMOS linear image sensor (Hamamatsu S8378) tilted to accommodate the locus of the foci of different wavelengths. The incoming light, after passing through the slit and being collected, dispersed and focused by the G-Fresnel, form a spectrum on the image sensor. The detected signal was subsequently digitized by a peripheral-component-interconnect-based data acquisition device (NI, PCI-6251) and analyzed in LabVIEW. To calibrate the spectrometer, an argon ion laser (Melles Griot 532-GS-A01) which lases at multiple wavelengths was focused into the entrance slit and had its spectrum measured.

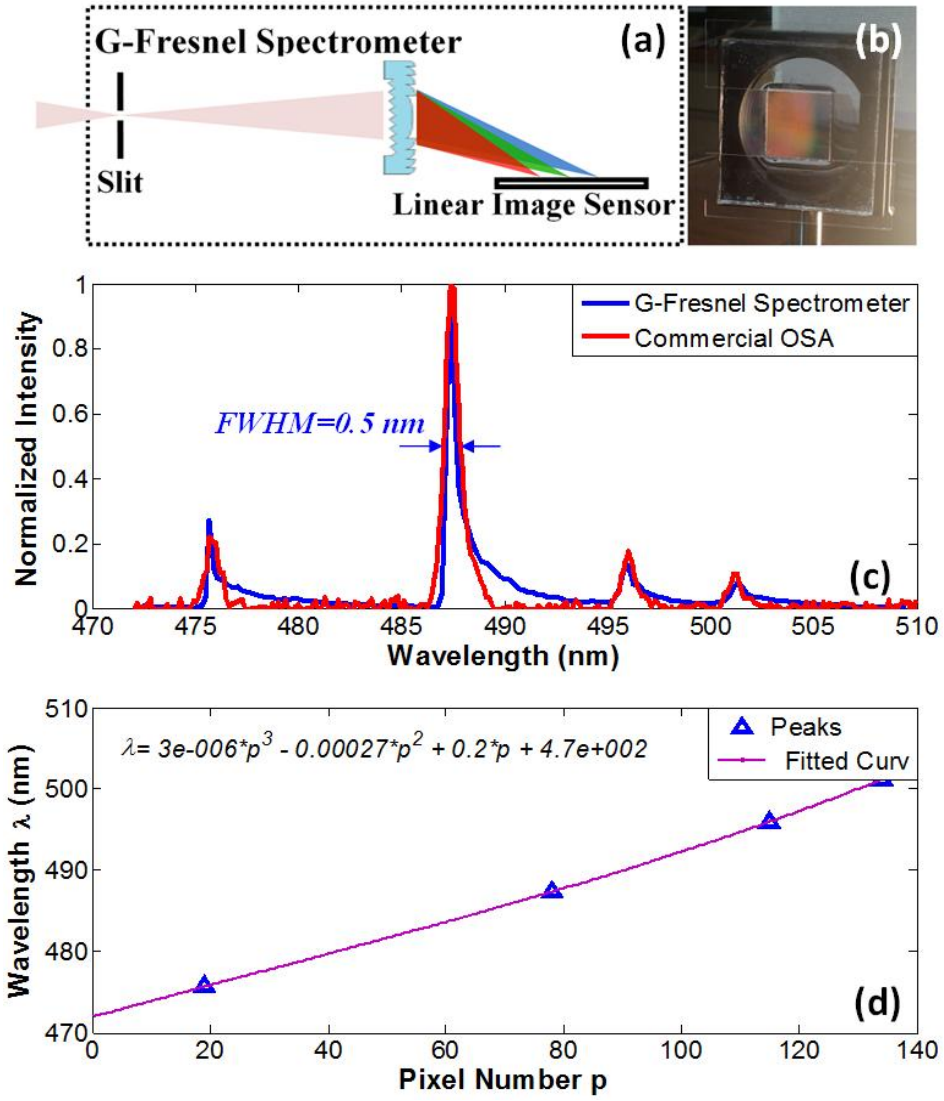

Figure 4.3.3 (a) Schematic diagram of the G-Fresnel spectrometer; (b) Mounted G-Fresnel device; (c) Partial spectrum of an argon ion laser measured by the G-Fresnel spectrometer (blue) and a commercial optical spectrum analyzer (red); (d) Calibrated pixel-wavelength.

By comparing the normalized spectrum measured by our G-Fresnel spectrometer [Fig.4.3.3 (c), blue] with the one obtained from a commercial optical spectrum analyzer (ANDO AQ-6315E, spectral resolution, 0.5 nm, Fig.4.3.3 (c),red), the pixel-wavelength relation of our spectrometer can be calibrated by having the

four peaks aligned as shown in Fig.4.3.3 (c). The relation can be fitted by a cubic polynomial function (Fig.4.3.3 (d)). Note that the FWHM measured in Fig.4.3.3 (c) shows that this spectrometer has a sub-nm spectral resolution. Next, we used this calibrated G-Fresnel spectrometer to characterize a laser-line filter (THORLABS FL488-10, CWL=488 $\pm$2 nm, FWHM=10 $\pm$2 nm) and a long-pass filter (CHROMA HQ485LP). To this end, a white light source (ROI 150 Illuminator) was utilized to illuminate the filters. The transmitted light was focused onto the entrance slit. The normalized transmission spectra of the laser-line filter and the long-pass filter measured by our spectrometer were shown in Fig.4.3.4 (blue curve). For comparison, we also measured the filter transmission spectra (red) by using a commercial high-resolution spectrograph with a liquid nitrogen cooled charge coupled device camera (PI/Acton SpectraPro 2500, spectral resolution: 0.09 nm). These measured results agree with each other well except that the long wavelength side of the point spread function measured by the G-Fresnel spectrometer shows a slowly decaying tail (Fig.4.3.3 (c)), which leads to noticeable deviations as can be observed in Fig.4.3.4 (c). This is likely due to the aberration introduced by the G-Fresnel and possible fabrication errors, which could be mitigated by improved fabrication accuracy and post-measurement data processing.

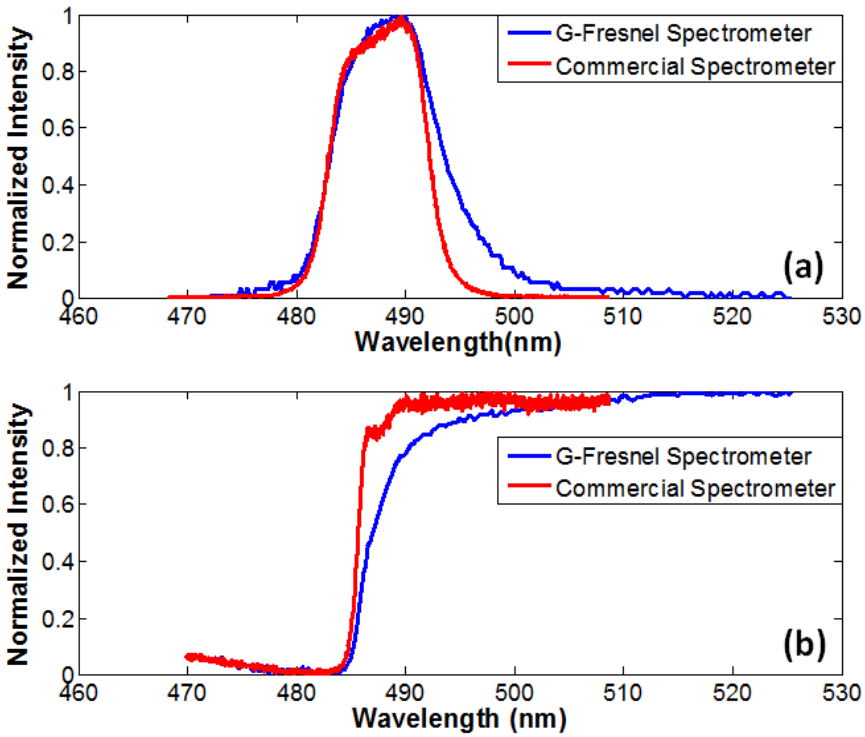

Figure 4.3.4 Measured transmission spectrum of a laser-line filter (a) and a long-pass filter (b); Blue curves: measured by the G-Fresnel spectrometer; Red curves: measured by a high-resolution commercial spectrograph.

So far we have demonstrated a G-Fresnel based spectrometer with near 1 nm resolution. However, this spectrometer relied on a transmission configuration that extended the dimensions of the device. Here, we investigate a version of the G-Fresnel spectrometer in which the G-Fresnel is utilized in a reflection configuration (reflection-type, R-G-Fresnel - Fig.4.3.5 (a)). A photo of a prototype version of the R-G-Fresnel spectrometer is shown in Fig.4.3.5 (b). Instead of imaging the transmitted spectrum from the back side of the G-Fresnel, a linear imaging sensor is placed adjacent and nearly perpendicular to the G-Fresnel on the entrance slit side of

the spectrometer to image the reflected signal. Due to the refractive index difference between PDMS [77] and air, a portion of the incident light is reflected by the PDMS-air interface of the grating pattern at the back side of the G-Fresnel and is collected on the linear imaging sensor. Since the reflected light propagates through the Fresnel pattern of the G-Fresnel twice, the effective focal length is thus reduced to one-half of its original value ($f_{eff}=f_o/2$). Therefore, both the entrance slit and the linear imager can be positioned significantly closer to the G-Fresnel in addition to the fact that the system is folded, reducing the overall dimension of the spectrometer.

Several measurements were performed to characterize and demonstrate the R-G-Fresnel spectrometer. Fig.4.3.5 (c) compares measurements of an argon ion laser source using a commercial spectrometer (PI/Acton SpectraPro 2500i, Spec-10 LN-cooled CCD, 150 grooves/mm 500 nm blazed grating, 10 μm entrance slit) and the R-G-Fresnel spectrometer (300 grooves/mm grating) over a 100 nm band from 440-540 nm. Both measurements are normalized and background-subtracted for comparison. It is observed that each of the Argon lines measured by the commercial spectrometer are visible in the R-G-Fresnel spectrum and align well in comparing wavelength. The difference in the line width measured by the R-G-Fresnel spectrometer can be attributed to a larger entrance slit and a ghosting effect from additional out of focus reflection orders that overlap the spectra. In future designs, the G-Fresnel device can be optimized to reduce these high-order reflections. In

Fig.4.3.5 (d), the known lines for the Argon laser source were used to obtain the wavelength calibration curve for the R-G-Fresnel device.

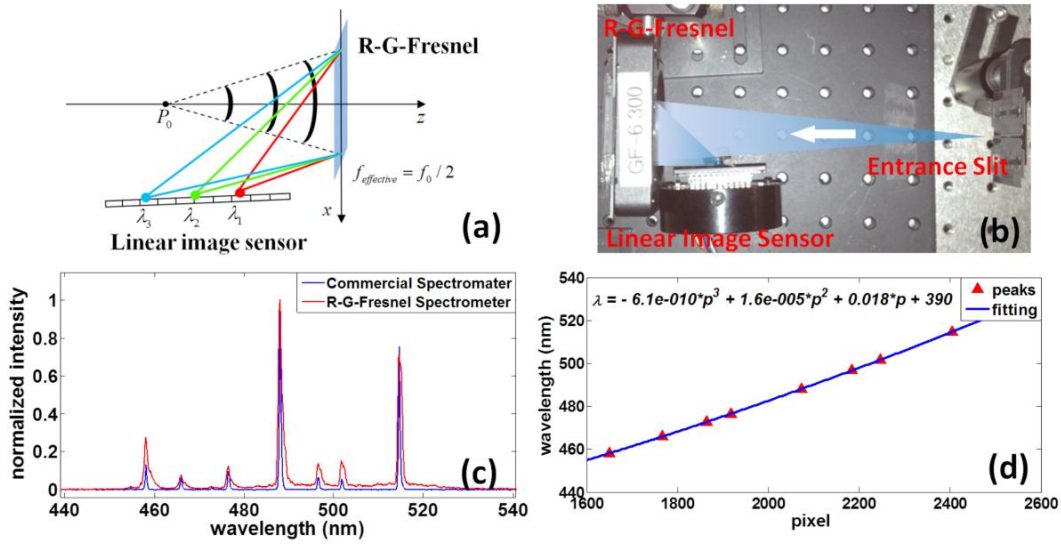

Figure 4.3.5 Reflection-type G-Fresnel spectrometer (a) Schematic of the R-G-Fresnel spectrometer. The effective focal length is reduced in half when compared to the transmission type G-Fresnel spectrometer. The overall dimension of the R-G-Fresnel spectrometer can be significantly reduced in this configuration. (b) A photo of the proof of concept R-G-Fresnel based spectrometer showing an entrance slit, the G-Fresnel device, and imaging sensor; (c) Argon-Ion laser spectrum acquired by a commercial spectrometer (blue) and the R-G-Fresnel based spectrometer (red) is compared; (d) calibration curve for linear imaging sensor using peak locations from Argon-Ion laser source.

To test the performance of this calibrated G-Fresnel spectrometer, we measured the spectral transmittance of a band-pass filter (HORIBA Scientific XB88 520BP10, CWL=520 nm) with incoherent white light illumination (ROI 150 Illuminator). Fig.4.3.6 plots the normalized, background-subtracted transmittance function as measured by the commercial spectrometer and the R-G-Fresnel spectrometer. The full-width-half-maximum (FWHM) of each measured filter

function is within 0.3 nm of each another; however, the commercial spectrometer detected a stronger feature at ~517 nm and at longer wavelengths the R-G-Fresnel based spectrometer had an elevated background.

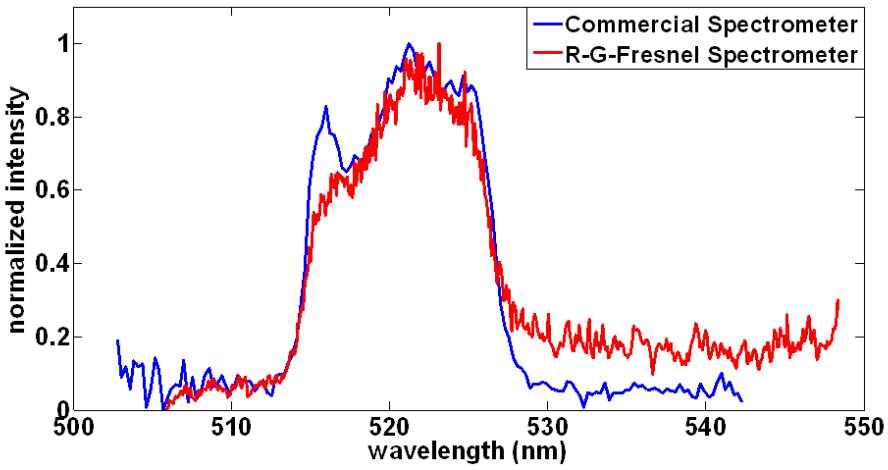

Figure 4.3.6 The transmittance of a 520 nm band pass filter is measured by a commercial spectrometer and R-G-Fresnel spectrometer.

In order to realize a high-efficiency reflection-type G-Fresnel, the grating side of the G-Fresnel lens needs to be highly reflective. We have explored the use of a thin layer of liquid metal alloy as a reflective coating. We first treated the grating surface of a G-Fresnel with plasma (METROLINE M4L Plasma Etcher) for 16 seconds, and then coated it with Galinstan (68.5% Ga, 21.5% In and 10% Sn by weight, GalliumSource). A photo of a coated G-Fresnel installed on an optical mount is shown in Fig.4.3.7.

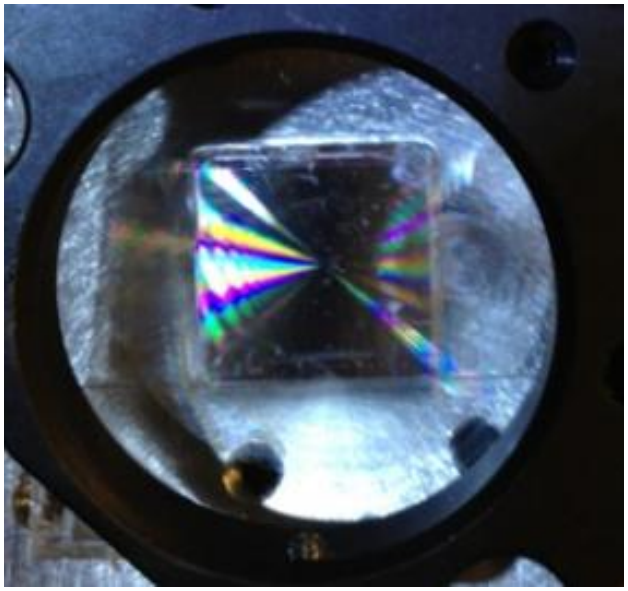

Figure 4.3.7 A photo of a reflection-type G-Fresnel coated with liquid metal.

Spectroscopic measurements were then performed by using the coated G-Fresnel in the reflection spectrometer configuration described previously (c.f., Fig.4.3.5 (a)). The measured spectrum of the argon-ion laser is plotted in Fig.4.3.8 (a). To suppress the effects from ghosting and separate the out-of-focus orders, the G-Fresnel was slightly shifted and was off-centered during the experiment. In Fig.4.3.8 (b), the calibration curve for the wavelength-pixel relationship is shown for the coated R-G-Fresnel spectrometer. In another performance comparison between the R-G-Fresnel spectrometer and a commercial grade spectrometer, we measured the fluorescence spectrum from an LED source in Fig.4.3.8 (c). The R-G-Fresnel spectrometer compared well over its available spectral range (R-G-Fresnel has a grating groove density of 300 gr/mm compared to the commercial spectrometer 150 gr/mm).

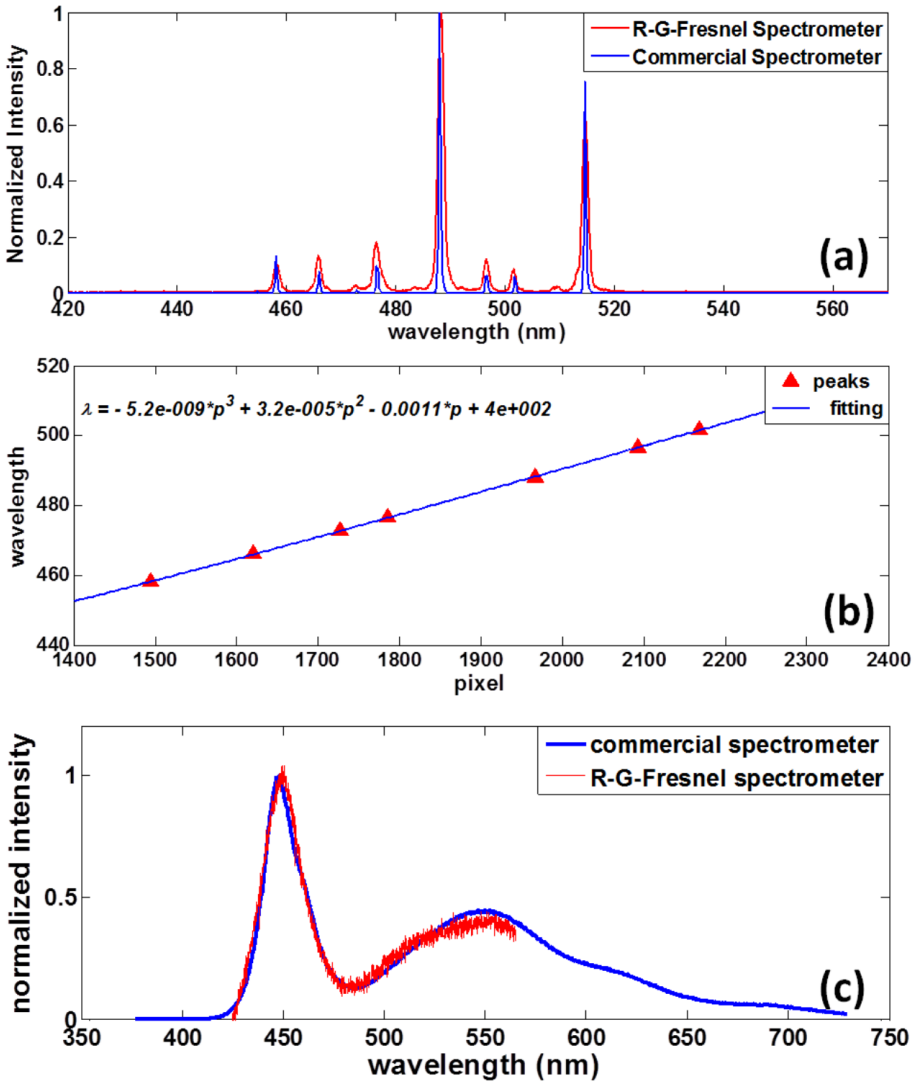

Figure 4.3.8 Liquid metal coated reflection type G-Fresnel. (a): captured Argon-Ion laser spectrum using the R-G-Fresnel spectrometer with a liquid metal coating on the G-Fresnel backside grating surface. (b): relationship between pixel and wavelength for the R-G-Fresnel spectrometer. (c): spectrum from an LED source measured by the liquid metal coated R-G-Fresnel spectrometer and compared to the spectrum captured by a commercial spectrometer.

Fluorescence spectroscopy experiment is also carried out with our coated RGF spectrometer prototype. The argon ion laser lasing at multiple wavelengths is

first filtered by a short pass filter and focused on fluorescent microspheres air dried on a piece of cover glass (Thermo Scientific Fluoro-Max Dyed Green, fluorescence emission peak at 509 nm). The pump and fluorescence are measured separately by the coated RGF spectrometer and the spectrum curves are plotted in a same frame in Fig.4.3.9, according to which the measured emission spectrum matches with the product specifications well.

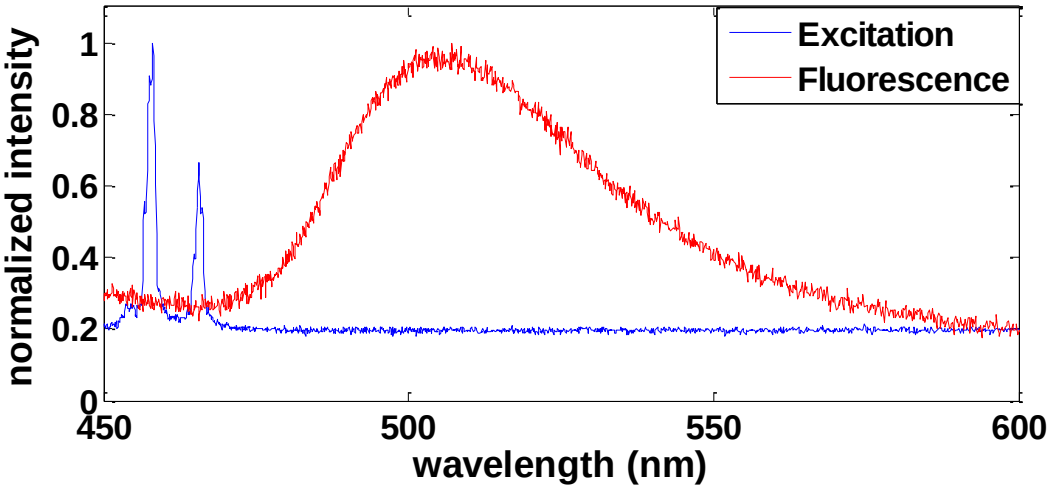

Figure 4.3.9 Spectrum of fluorescent microspheres excited by argon-ion laser. The blue is excitation spectrum and the red is the fluorescence spectrum. The excitation spectrum and the fluorescence spectrum are normalized respectively.

In summary, a millimeter-sized G-Fresnel was demonstrated, based upon which a compact optical spectrometer was proposed. Our analysis shows that, despite a compact dimension, a spectral resolution of ~1 nm can be potentially achieved. We also experimentally demonstrated different configurations of proof-of-concept G-Fresnel-based spectrometers with satisfying spectral resolution. Our

results indicate that the G-Fresnel promises a new way towards spectrometer miniaturization. We believe that this type of low-cost and miniature spectrometer can potentially find a variety of applications and can be integrated with mobile devices as well as lab-on-a-chip devices, opening an economical avenue for mobile and on-chip optical spectroscopy.

4.4 Future development of the G-Fresnel spectrometer

The future development of our G-Fresnel spectrometer will be mainly focusing on two parts: one is to further minimize the dimension of the spectrometer and the other is to improve the material used for the fabrication of the diffractive optical element.

To further reduce the dimension of our existing prototype, first of all the design focal length can be shortened to the order of cm or even mm. According to our simulation [78], a 4 mm × 4 mm G-Fresnel with designed focal length 10 mm can still achieve spectral resolution as high as 1nm. The progress of nanotechnologies, especially the focused ion beam etching technique, have enabled the direct etching of μm-size G-Fresnel features onto the surface of a silicon wafer to form the mold used for soft-lithography.

PDMS has been proved to be an applicable material for the prototype of G-Fresnel diffractive optical element due to its good optical properties, low cost and easy handling. However, there are still some issues existing. For example, the ultra-

low surface energy makes it very difficult to be coated with metal. Also it has too much flexibility in the shape, complicating the mounting of the optical elements. In the future stage of volume production, some other materials might be tested for this application. For example, silk optics was proposed by Fiorenzo Omenetto and David Kaplan in Tufts University [79]. In their demonstration, the silk could be used to fabricate various optical elements, and its mechanical and optical properties are far better than PDMS.

CHAPTER 5. CONCLUSION AND FUTURE WORK

This dissertation is mainly focused on advanced nonlinear imaging and spectroscopy techniques. In particular, the work of improving the speed of two-photon fluorescence and second harmonic microscopy by employing special diffractive optical elements (DOEs) and nanotechnologies is discussed in the first part. To further optimize the performance of not only the nonlinear imaging, but also a broad range of applications in which laser-material interactions matters, ultrashort laser pulse characterization is an indispensable tool. In the second part of the dissertation, a new method of spatiotemporal characterizations of ultrashort laser pulse at nano-femto resolution is proposed and demonstrated. Spectroscopy has been the most critical tool for optics and many other fields in both academic research and industry. So as the last part of this dissertation, an interesting solution for miniaturization of spectrometers is proposed and demonstrated.

Comparing to the conventional one-photon fluorescence imaging microscopy, two-photon fluorescence excitation microscopy has multiple obvious advantages, including deeper penetration depth, less damage to biological specimen and inherent optical sectioning capability. However, slow mechanical scanning during the three-dimension imaging is usually necessary and hindering its role in real-time applications like monitoring dynamic processes. To overcome this problem, in the

chapter 2 of this dissertation, we explored a chromatic imaging technique, which takes advantage of the chromatic aberration of a Fresnel lens to eliminate mechanical scanning along the axial direction. For a Fresnel lens, the focal length F and the wavelength λ have a relationship $\lambda F = \lambda_0 F_0$, in which λ_0 and F_0 are the design wavelength of the Fresnel lens and its corresponding focal length, respectively. As a result, different wavelengths of an input pulse can be focused to different axial positions to generate fluorescence signals in parallel. Then a method of "z-microscopy" by utilizing an array of 45°-tilted micro mirrors arranged along the axial direction was implemented. Image signals emitted from different axial positions can be orthogonally reflected by the corresponding micro mirrors and spatially separated for parallel detection, essentially converting the more challenging axial imaging to a lateral imaging problem. Each micro mirror also provides optical sectioning capability due to its finite dimension. Numerical analysis shows that nearly diffraction limited axial resolution can be achieved. Experimental demonstration of z-imaging of fluorescent microspheres is also presented. In addition, for the case of second harmonic imaging microscopy, with a similar excitation setup, frequency-doubled second harmonic signals at different center wavelengths are generated at different depths in parallel. Thus different axial positions can be resolved in parallel by performing a spectroscopic measurement.

Next, in order to optimize the performance of the nonlinear imaging microscopy and many other related applications including coherence control, laser micromachining and laser troubleshooting, a new approach for spatiotemporal characterization of the ultrashort laser pulse with nano-femto resolution is proposed and demonstrated. This approach has been applied to the investigation of the pulse propagation through the vicinity of the focal point of an objective lens, and phase and shape information of the pulse and its evolution can be revealed.

At the end, optical spectroscopy is an indispensable analytical tool used in a wide variety of scientific fields. Spectroscopic instruments are usually limited to use in the laboratory setting as these devices are typically bulky and costly due to the employment of discrete optical components. In the last part of this thesis, a hybrid diffractive optical element G-Fresnel was demonstrated, which integrates the functionalities of a grating and a Fresnel lens. The advantages of the G-Fresnel are three-fold: first, it combines the functions of collimation, dispersion and collection in a single thin-film element; second, it can have a low f-number, leading to a compact system; third, it may be realized by surface relief patterning, opening the possibility of low-cost volume production through replicating from a master pattern. Here we explore the G-Fresnel based optical spectrometer both theoretically and experimentally. Our simulation shows that a spectral resolution of about 1 nm can be achieved by using a compact G-Fresnel (diameter ~ 4 mm, focal length, 1 cm). A

proof-of-concept spectrometer implemented with a G-Fresnel is also experimentally demonstrated.

As possible directions for future research work based on the solutions and results described in this dissertation, more efforts may be devoted to the following several topics.

First, for the nonlinear imaging microscopy research, particularly for the project 'Z-Microscopy', the matching between the specifications of the applied optics and the micro mirror array device is still far from satisfying. More detailed simulations are demanded and the fabrication process (photolithography) needs to be further improved for more accurate dimensions and higher aspect ratio. With the improvement of this technique, a high-quality 3D image of a real biological sample is expected to be achieved.

Second, the next step for the holographic collinear FROG project is to employ the previously developed nanoprobe technology to implement the near field pulse characterization with the help of a near-field optical microscopy (NSOM) system. Many more interesting and exciting demonstrations are expected.

At the end, a complete prototype of the G-Fresnel spectrometer including a proper linear CMOS and the necessary electronics should be constructed for more demonstrations. Meanwhile, we are currently collaborating with some other groups

to fabricate next-generation G-Fresnel device at the scale in the order of micro meters and with better material.

BIBLIOGRAPHY:

[1] Y. R. Shen, *The principles of nonlinear optics* (Wiley-Interscience, New York, USA, 1984).

[2] M. Göppert-Mayer, "Über Elementarakte mit zwei Quantensprüngen," Ann. Phys. **9**, 273–294 (1931).

[3] W. Kaiser, and C. G. B. Garrett, "2-Photon Excitation in Caf2 - Eu2+," Phys. Rev. Lett. **7**, 229-& (1961).

[4] C. J. R. Sheppard, J. N. Gannaway, R. Kompfner, and D. Walsh, "Scanning Harmonic Optical Microscope," IEEE J. Quantum Elect. **13**, D100-D100 (1977).

[5] W. Denk, J. H. Strickler, and W. W. Webb, "2-Photon Laser Scanning Fluorescence Microscopy," Science **248**, 73-76 (1990).

[6] Sheetz, K. E., Hoover, E. E., Carriles, R., Kleinfeld, D., & Squier, J. A., "Advancing multifocal nonlinear microscopy: development and application of a novel multibeam Yb: KGd (WO4) 2 oscillator." Opt. Express, **16**, 22 (2008).

[7] D. Meshulach, D. Yelin, and Y. Silberberg, "Adaptive real-time femtosecond pulse shaping," J. Opt. Soc. Am. B 15, 1615-1619 (1998).

[8] Dayan, Barak, Avi Pe'Er, Asher A. Friesem, and Yaron Silberberg. "Two photon absorption and coherent control with broadband down-converted light." *Physical review letters* 93, **2** (2004).

[9] Dela Cruz, Johanna M., Igor Pastirk, Matthew Comstock, Vadim V. Lozovoy, and Marcos Dantus. "Use of coherent control methods through scattering biological tissue to achieve functional imaging." *Proceedings of the National Academy of Sciences of the United States of America* 101, **49** (2004).

[10] Ogilvie, Jennifer P., Delphine Débarre, Xavier Solinas, Jean-Louis Martin, Emmanuel Beaurepaire, and Manuel Joffre. "Use of coherent control for selective two-photon fluorescence microscopy in live organisms." *Optics Express* 14, **2** (2006).

[11] Hosseini, S. Abbas, and Debabrata Goswami. "Coherent control of multiphoton transitions with femtosecond pulse shaping." *Physical Review A* 64, **3** (2001).

[12] Stoian, R., M. Boyle, A. Thoss, A. Rosenfeld, G. Korn, and I. V. Hertel. "Dynamic temporal pulse shaping in advanced ultrafast laser material processing." *Applied Physics A* 77, no. 2 (2003): 265-269.

[13] Rick Trebino (2002). *Frequency-Resolved Optical Gating: The Measurement of Ultrashort Laser Pulses*. Springer. ISBN 1-4020-7066-7.

[14] R. Trebino, K. W. DeLong, D. N. Fittinghoff, J. N. Sweetser, M. A. Krumbügel, and D. J. Kane, "Measuring Ultrashort Laser Pulses in the Time-Frequency Domain Using Frequency-Resolved Optical Gating," *Review of Scientific Instruments* **68**, 3277-3295 (1997).

[15] A. Baltuska, M. S. Pshenichnikov, and D. A.Wiersma "Amplitude and phase characterization of 4.5-fs pulses by frequency-resolved optical gating," *Opt. Lett.* **23**, 1474-1476 (1998).

[16] Nesci, Antonello, René Dändliker, and Hans Peter Herzig. "Quantitative amplitude and phase measurement by use of a heterodyne scanning near-field optical microscope." *Opt. Lett.* 26, **4** (2001).

[17] Phillips, P. L., J. C. Knight, J. M. Pottage, G. Kakarantzas, and P. St J. Russell. "Direct measurement of optical phase in the near field." *Applied physics letters* 76, **5** (2000).

[18] Amat-Roldán, I., Cormack, I. G., Loza-Alvarez, P., Gualda, E. J., & Artigas, D. "Ultrashort pulse characterisation with SHG collinear-FROG," *Opt. Express*, ***12***, 6, (2004)

[19] C. Yang, K. Shi, P. Edwards, and Z. Liu, "Demonstration of a PDMS based hybrid grating and Fresnel lens (G-Fresnel) device," *Opt. Express* **18**, 23529-23534 (2010).

[20] S. Ram, P. Prabhat, E. S. Ward, and R. J. Ober, "Improved single particle localization accuracy with dual objective multifocal plane microscopy." Opt. Express **17**, 6881 (2009).

[21] P. Prabhat, Z. Gan, J. Chao, S. Ram, C. Vaccaro, S. Gibbons, R. J. Ober, and E. S. Ward, "Elucidation of intracellular recycling pathways leading to exocytosis of the Fc receptor, FcRn, by using multifocal plane microscopy." Proc. Natl. Acad. Sci. USA **104**, 5889 (2007).

[22] J. Rosen and G.Brooker, "Non-scanning motionless fluorescence three-dimensional holographic microscopy." *Nat. Photon.* **2**, 190 (2008).

[23] W. Amir, R. Carriles, E. E. Hoover, T. A. Planchon, C. G. Durfee, and J. A. Squier, "Simultaneous imaging of multiple focal planes using a two-photon scanning microscope," *Opt. Lett.* **32**, 1731-1733 (2007).

[24] Goodman, Joseph. "Introduction to Fourier optics." (2008).

[25] Q. Xu, K. Shi, S. Yin, and Z. Liu, "Chromatic two-photon excitation fluorescence imaging," *J. Microsc.* **235**(1), 79–83 (2009).

[26] Franken, P., Hill, A., Peters, C., Weinreich, G. "Generation of Optical Harmonics," *Phys. Rev. Lett.* **7** (4), 118 (1961).

[27] Boyd, Robert W. "Nonlinear optics." (1992).

[28] J. N. Gannaway and C. J. R. Sheppard, "Second-harmonic imaging in the scanning optical microscope," *Opt. Quantum Electron.* **10**, 5, 435–439 (1978).

[29] L. Moreaux, O. Sandre, and J. Mertz, "Membrane imaging by second-harmonic generation microscopy," *J. Opt. Soc. Am. B* **17**, 10, 1685–1694 (2000).

[30] P. J. Campagnola and L. M. Loew, "Second-harmonic imaging microscopy for visualizing biomolecular arrays in cells, tissues and organisms," *Nat. Biotechnol.* **21,** 11, 1356–1360 (2003).

[31] W. R. Zipfel, R. M. Williams, R. Christie, A. Y. Nikitin, B. T. Hyman, and W. W. Webb, "Live tissue intrinsic emission microscopy using multiphoton-excited native fluorescence and second harmonic generation," *Proc. Natl. Acad. Sci.* **100**, 12, 7075–7080 (2003).

[32] E. Brown, T. McKee, E. diTomaso, A. Pluen, B. Seed, Y. Boucher, and R. K. Jain, "Dynamic imaging of collagen and its modulation in tumors in vivo using second-harmonic generation," Nat. Med. **9,** 6, 796–801 (2003).

[33] G. Molesini, G. Pedrini, P. Poggi, and F. Quercioli, "Focus-wavelength encoded optical profilometer," Opt. Commun. **49**(4), 229–233 (1984).

[34] S. L. Dobson, P. C. Sun, and Y. Fainman, "Diffractive lenses for chromatic confocal imaging," Appl. Opt. **36**(20), 4744–4748 (1997).

[35] K. Shi, P. Li, S. Yin, and Z. Liu, "Chromatic confocal microscopy using supercontinuum light," Opt. Express **12**(10), 2096–2101 (2004).

[36] K. Shi, S. H. Nam, P. Li, S. Yin, and Z. Liu, "Wavelength division multiplexed confocal microscopy using supercontinuum," Opt. Commun. **263**(2), 156–162 (2006).

[37] K. Shi, S. Yin, and Z. Liu, "Wavelength division scanning for two-photon excitation fluorescence imaging," J. Microsc. **223**(2), 83–87 (2006).

[38] F. T. S. Yu, Introduction to diffraction, information processing, and holography (MIT Press, Cambridge, MA, (1973)).

[39] K. Shi, Supercontinuum imaging and spectroscopy, Penn State Doctoral Dissertation (2007).

[40] E. Hecht, *Optics* (Addison Wesley, 2001).

[41] A. Einstein,"On the quantum theory of radiation," *Phys. Z* **18** (1917).

[42] Maiman, T. H. “Stimulated optical radiation in ruby,” (1960).

[43] Muller, M., et al. "Dispersion pre-compensation of 15 femtosecond optical pulses for high-numerical-aperture objectives." *Journal of microscopy* 191.2 (1998): 141-150.

[44] Squier, Jeff, and Michiel Muller. "High resolution nonlinear microscopy: A review of sources and methods for achieving optimal imaging." *Review of Scientific Instruments* 72.7 (2001): 2855-2867.

[45] Zipfel, Warren R., Rebecca M. Williams, and Watt W. Webb. "Nonlinear magic: multiphoton microscopy in the biosciences." *Nature biotechnology* 21.11 (2003): 1369-1377.

[46] Meshulach, Doron, and Yaron Silberberg. "Coherent quantum control of two-photon transitions by a femtosecond laser pulse." *Nature* 396.6708 (1998): 239-242.

[47] V. V. Lozovoy, I. Pastirk, and M. Dantus, "Multiphoton intrapulse interference 4: Characterization and compensation of the spectral phase of ultrashort laser pulses," Optics Letters 29, 775-777 (2004).

[48] B. Xu, J. M. Gunn, J. M. Dela Cruz, V. V. Lozovoy, M. Dantus, “Quantitative investigation of the MIIPS method for phase measurement and compensation of femtosecond laser pulses,” J. Optical Society of America B 23, 750-759 (2006).

[49] US patent 6611336, Ian A. Walmsley & Chris Iaconis, "Pulse measurement using frequency shifting techniques", issued 2003-8-26

[50] Iaconis, C; Walmsley, I. A. (1999), "Self-Referencing Spectral Interferometry for Measuring Ultrashort Optical Pulses",*IEEE J. Quantum Electron.* **35** (4): 501–509, Bibcode:1999IJQE...35..501I, doi:10.1109/3.753654

[51] Iaconis, C; Walmsley, I. A. (1998), "Spectral Phase Interferometry for Direct Electric-Field Reconstruction of Ultrashort Optical Pulses", *Opt. Lett.* **23** (10): 792–794, Bibcode:1998OptL...23..792I, doi:10.1364/OL.23.000792,PMID 18087344

[52] Walmsley, I. A.; Wong, V. (1996), "Characterization of the Electric Field of Ultrashort Optical Pulses", *J. Opt. Soc. Am. B* **13** (11):

[53] Extermann, Jerome, et al. "Nano-FROG: Frequency resolved optical gating by a nanometric object." *Opt. Express* 16.14 (2008): 10405-10411.

[54] Rulli ère, C. (Ed.). (2005). *Femtosecond laser pulses: principles and experiments*. Springer Science+ Business Media.

[55] Amat-Rold án, I., Cormack, I. G., Loza-Alvarez, P., Gualda, E. J., & Artigas, D., "Ultrashort pulse characterisation with SHG collinear-FROG," Opt. Express, **12**, 6, (2004)

[56] Nesci, Antonello, Ren é D ändliker, and Hans Peter Herzig. "Quantitative amplitude and phase measurement by use of a heterodyne scanning near-field optical microscope," *Opt. Letters* **26**, 4 (2001).

[57] Phillips, P. L., J. C. Knight, J. M. Pottage, G. Kakarantzas, and P. St J. Russell. "Direct measurement of optical phase in the near field." Applied physics letters 76, **5** (2000).

[58] Li, Haifeng, Zhe Zhang, Qian Xu, Kebin Shi, Yaoshun Jia, Baigang Zhang, Yong Xu, and Zhiwen Liu. "Characterizing ultrashort optical pulses using second-order nonlinear nanoprobes." Applied Physics Letters 97, **26** (2010).

[59] Stibenz, Gero, and G ünter Steinmeyer. "Interferometric frequency-resolved optical gating." *Optics Express* 13, 7 (2005).

[60] William Hyde Wollaston (1802) "A method of examining refractive and dispersive powers, by prismatic reflection," Philosophical Transactions of the Royal Society, 92: 365 ¨C380; see especially p. 378.

[61] Herschel, William (1800). "Experiments on the Refrangibility of the Invisible Rays of the Sun". Philosophical Transactions of the Royal Society of London 90: 284 ¨C292. doi:10.1098/rstl.1800.0015. JSTOR 107057.

[62] Reprinted, with additional findings and notes, in: Joseph Fraunhofer (1817) "Bestimmung des Brechungs- und des Farben-Zerstreuungs - Verm?gens verschiedener Glasarten, in Bezug auf die Vervollkommnung achromatischer Fernr?hre" (Determination of the refractive and color-dispersing power of different types of glass, in relation to the improvement of achromatic telescopes), Annalen der Physik, 56: 264-313; see especially pages 278-286.

[63] G. Kirchhoff (1860). "Ueber das Verh?ltniss zwischen dem Emissionsverm?gen und dem Absorptionsverm?gen der K?rper f ¨r W?rme und Licht". Annalen der Physik 185 (2): 275 ¨C301. Bibcode:1860AnP...185..275K. doi:10.1002/andp.18601850205.

[64] C. Palmer, and E. Loewen, Diffraction grating handbook (Newport Corporation, 2005).

[65] C. Hsieh, O. Momtahan, A. Karbaschi, A. Adibi, “Compact Fourier-transform volume holographic spectrometer for diffuse source spectroscopy,” Opt. Lett. 30(8), 836–838 (2005).

[66] Lammel, G.; Schweizer, Sandra; Renaud, P., "MEMS infrared gas spectrometer based on a porous silicon tunable filter," Micro Electro Mechanical Systems, 2001. MEMS 2001. The 14th IEEE International Conference (2001).

[67] S. Camou, H. Fujita, and T. Fujii, “PDMS 2D optical lens integrated with microfluidic channels: principle and characterization,” Lab Chip **3**(1), 40–45 (2003).

[68] D. A. Chang-Yen, R. K. Eich, and B. K. Gale, “A Monolithic PDMS Waveguide System Fabricated Using SoftLithography Techniques,” J. Lightwave Technol. **23**(6), 2088–2093 (2005).

[69] F. Schneider, J. Draheim, R. Kamberger, and U. Wallrabe, “Process and material properties of polydimethylsiloxane (PDMS) for Optical MEMS,” Sens. Actuators, A **151**(2), 95–99 (2009).

[70] J. A. Rogers, and R. G. Nuzzo, “Recent progress in soft lithography,” Mater. Today **8**(2), 50–56 (2005).

[71] Born, M., & Wolf, E. (1999). *Principles of optics: electromagnetic theory of propagation, interference and diffraction of light*. CUP Archive.

[72] J. A. Rogers, and R. G. Nuzzo, “Recent progress in soft lithography,” Mater. Today **8**(2), 50–56 (2005)

[73] J. K. Ranka, R. S. Windeler, and A. J. Stentz, “Visible continuum generation in air-silica microstructure optical fibers with anomalous dispersion at 800 nm,” *Opt. Lett.* **25**(1), 25–27 (2000)

[74] J. C. Knight, T. A. Birks, P. S. Russell, and D. M. Atkin, “All-silica single-mode optical fiber with photonic crystal cladding,” *Opt. Lett.* **21**(19), 1547–1549 (1996).

[75] Y. Fainman, L. P. Lee, D. Psaltis, and C. Yang, Optofluidics-Fundamentals, Devices and Applications (McGrawHill, 2010).

[76] K. Shi, “Imaging and spectroscopy,” Ph.D. dissertation (Pennsylvania State University, 2007).

[77] D. A. Chang-Yen, R. K. Eich and B. K. Gale, J. Lightwave Technol. 23, 2088(2005).

[78] C. Yang, P. Edwards, K. Shi, and Z. Liu, "Proposal and demonstration of a spectrometer using a diffractive optical element with dual dispersion and focusing functionality," Opt. Lett. 36, 2023-2025 (2011).

[79] Omenetto, F. G., & Kaplan, D. L., "A new route for silk,". *Nat. Photonics **2***, 11. (2008).

VITA

CHUAN YANG

EDUCATION

- Ph.D. in Electrical Engineering with focus in Optics (GPA 3.8/4.0), Aug. 2013
  The Pennsylvania State University, University Park, PA 16802
- M.S. in Physics with focus in laser optics (GPA 3.8/4.0), May 2008
  University of Pittsburgh, Pittsburgh, PA 15260

PUBLICATIONS

Peer-review journals:

[1] **C. Yang**, M. Zhou, S. Zheng, S. Yin, Z. Liu, "Z-microscopy for parallel axial imaging with micro mirror array," *Appl. Phys. Lett.* **101**, 231111 (2012).

[2] H. Li, D. Ma, **C. Yang**, Z. Liu, "Incorporating conductive materials into a photonic crystal fiber: toward optoelectronic applications," *Opt. Express* **20**, 24342 (2012).

[3] **C.Yang**, P. Edwards, K. Shi, and Z. Liu, "Proposal and demonstration of a spectrometer using a diffractive optical element with dual dispersion and focusing functionality," *Opt. Lett.* **36**, 2023-2025 (2011).

[4] M. Zhou, **C. Yang**, Z. Liu, J. P. Cysyk and S. Zheng, "An implantable Fabry-Perot pressure sensor fabricated on left ventricular assist device for heart failure," *Biomedical Microdevices,* **14**, 1, 235-245 (2011).

[5] **C. Yang**, K. Shi, P. Edwards, and Z. Liu, "Demonstration of a PDMS based hybrid grating and Fresnel lens (G-Fresnel) device," *Opt. Express* **18**, 23529-23534 (2010).

[6] **C. Yang**, K. Shi, H. Li, Q. Xu, V. Gopalan, and Z. Liu, "Chromatic second harmonic imaging," *Opt. Express* **18**, 23837-23843 (2010).

Conference proceedings:

[7] J. Ouyang, **C. Yang**, D. Niu, Y. Xie and Z. Liu, "F2BFLY: An On-Chip Free-Space Optical Network with Wavelength-Switching," *ICS '11* (2011).

[8] **C. Yang**, K. Shi, H. Li, Q. Xu, V. Gopalan, and Z. Liu, "Non-axial-scanning Second Harmonic Microscopy," in *CLEO: 2011 - Laser Applications to Photonic Applications,* OSA Technical Digest.

[9] M. Zhou, **C. Yang**, Z. Liu, J. P. Cysyk, and S. Zheng, "A Fabry-Perot pressure sensor fabricated on left ventricular assist device for heart failure implant," *Solid-State Sensors, Actuators and Microsystems Conference (TRANSDUCERS), 16th International,* 1232 - 1235 (5-9 June 2011).

[10] **C. Yang**, P. Edwards, K. Shi, and Z. Liu, "Hybrid Diffractive Optical Element Based Spectrometer," in *CLEO:2011 - Laser Applications to Photonic Applications*, OSA Technical Digest.

CONFERENCE PRESENTATIONS

- "Non-axial-scanning Second Harmonic Microscopy," CLEO, Baltimore (2011).
- "A compact optical spectrometer based on a single-grating Fresnel diffractive optical element," Oral Presentation, SPIE Defense, Security and Sensing, Baltimore (2012).

PATENTS

- **C. Yang**, *et al.* US Patent Application Publication titled, 'Compact spectrometer including a diffractive optical element with dual dispersion and focusing functionality', **Pub. No.: US2012/0038918A1** (2012).

AWARDS

- SPIE Optics and Photonics scholarship, SPIE, July 2012
- Invention Incentive Award, Penn State Research Foundation, August 2012
- A. J. Ferraro Ph.D. Research Award, The Pennsylvania State University, April 2012
- Vodafone wireless innovation project 3rd place winner, April 2013